POLITECNICO DI TORINO
Repository ISTITUZIONALE

Impact of radiator installation on noise reduction strategies for automotive engine cooling fans

Original
Impact of radiator installation on noise reduction strategies for automotive engine cooling fans / Bellelli, F., Arina, R., Avallone, F.. - In: INTERNATIONAL JOURNAL OF AEROACOUSTICS. - ISSN 1475-472X. - (2026). [10.1177/1475472x261473632]

Availability:
This version is available at: 11583/3013727 since: 2026-07-30T06:49:34Z

Publisher:
Sage

Published
DOI:10.1177/1475472x261473632

Terms of use:

This article is made available under terms and conditions as specified in the corresponding bibliographic description in the repository

Publisher copyright
Sage postprint/Author's Accepted Manuscript

(Article begins on next page)

14 September 2026

Impact of radiator installation on noise reduction strategies for automotive engine cooling fans

Francesco Bellelli*[1], Renzo Arina[1], and Francesco Avallone[1]

[1]Department of Mechanical and Aerospace Engineering, Politecnico di Torino, Torino, 10129, Italy.

March 20, 2026

Abstract

This study investigates, with high-fidelity numerical simulations, how the effectiveness of noise reduction technologies, conventionally developed and tested for isolated fans, is affected when they are coupled with a radiator since the influence of such installations on fan noise reduction technologies is still poorly documented. Two noise reduction strategies are investigated to reduce two different noise sources. The first aims at reducing the backflow by redesigning an ad-hoc rotating ring; the second aims at reducing rotor-stator interaction by optimizing the stator vanes azimuthal distribution with a genetic algorithm. In the isolated fan, the new ring reduces broadband noise by redirecting the backflow radially, achieving an Overall Sound Pressure Level (OASPL) reduction of 4 dBA. The optimized vane spacing further decreases tonal noise by up to 10 dBA. The new ring alters the operating point by increasing the volume flow rate by 6% while increasing the aerodynamic torque by 10% due to its larger aerodynamic surface. When the radiator is installed, the flow confinement caused by the radiator casing does not allow an effective backflow redirection with the new ring, resulting in an OASPL increase of 2 dBA, while vane spacing still suppresses tonal harmonics by up to 3 dBA. Aerodynamic performance remains within 3% of the baseline, thus being less sensitive to geometry modifications with respect to the isolated fan configuration. These results demonstrate that installation effects can significantly alter the effectiveness of fan noise reduction technologies and, if designed for a free-field environment, should therefore be considered at design.

Keywords: aeroacoustics; axial fan; Lattice-Boltzmann Method; noise reduction technologies; rotor-stator interaction; rotor-backflow interaction

*Corresponding author. Email: `francesco.bellelli@polito.it`

Nomenclature

$\bar{q}$	Mean of q
$\tilde{q}$	Fourier Transform of q
q_σ	Standard deviation of q
vox	Number of voxels in the finest VR region
Δx	Voxel size [m]
Δt	Timestep [s]
ν	Kinematic viscosity [m^2/s]
ρ	Density [kg/m^3]
$u_\tau = \frac{\tau_w}{\rho}$	Skin friction velocity [m/s]
$y^+ = \frac{u_\tau \Delta x}{\nu}$	Dimensionless wall distance [-]
M	Mach number [-]
ω	Vorticity [1/s]
x, y, z	Axial, horizontal, and vertical coordinates [m]
$r = \sqrt{y^2 + z^2}$	Radial position in the x plane
D	Fan diameter [m]
R_{tip}	Fan tip radius [m]
c	Blade chord [m]
Ω	Fan rotational speed [RPM]
B	Number of rotor blades [-]
N_v	Number of stator vanes [-]
f	Frequency [Hz]
BPF = $B\Omega$	Blade Passing Frequency [Hz]
p	Static pressure [Pa]
SPL = $20\log_{10}\left(\frac{p_{rms}}{2\cdot10^{-5}}\right)$	Sound Pressure Level [dBA]
OASPL = $10\log_{10}\left(\sum_i 10^{\frac{SPL(f_i)}{10}}\right)$	Overall Sound Pressure Level [dBA]
$\Delta p = p_{amb} - p$	Pressure rise [Pa]
$\dot{V}$	Volume flow rate across the fan [m^3/s]
Q	Aerodynamic torque [Nm]
$v_{tip} = \Omega\frac{D}{2}$	Tip velocity [m/s]
u, v_r, v_θ	Axial, radial, and tangential velocities [m/s]
$\psi = \frac{2\Delta p}{\rho v_{tip}^2}$	Load coefficient [-]
$\varphi = \frac{4\dot{V}}{\pi(D^2 - D_{hub}^2)v_{tip}}$	Flow coefficient [-]
T	Fan thrust [N]

1 Introduction

Automotive engines are cooled with fan modules, designed by prioritizing aerodynamic efficiency. However, with the transition to electric motors, the reduction of noise emissions has become a priority. This has led the scientific community to investigate various noise reduction technologies. Piwowarski and Jakowski (2023) provided a comprehensive review of approaches to enhance fan efficiency while reducing noise, whereas Zhou et al. (2023) focused on bionic-inspired solutions to mitigate aerodynamic

noise.

Engine cooling fans are characterized by many noise sources, which can be classified as airfoil self-noise, loading noise, and thickness noise. Some of them depend on the operating conditions (Longhouse 1976) and geometry of the blades (Brooks et al. 1989). In contrast, others depend on their installation within the cooling module (Bellelli et al. 2025a) and the presence of stator vanes (Sharland 1964). For low-speed fans, the monopolar contribution characterizing the thickness noise can be neglected (Caro and Moreau 2000), although it can play a significant role in the case of high-solidity fans, as found by Díaz et al. (2009); the quadrupolar sources due to the distortion or scattering of turbulent eddies, responsible for the airfoil self-noise, are usually negligible up to a tip Mach number of $M = 0.8$ (Moreau and Roger 2007; Morfey 1971). Therefore, in the nominal range of operations, the main noise contribution for low-speed fans is the loading noise, which exhibits a dipolar behavior in terms of directivity.

Two main phenomena generate loading noise: (i) if the blade loading is constant, then steady loading noise dominates, with the noise spectrum characterized by a tonal peak at the Blade Passing Frequency (BPF) equal to $B\Omega/60$ and its harmonics. In this case, the amplitude of the tonal peak decreases with increasing BPF harmonics. (ii) If the inflow is not uniform or turbulent, the blade loading varies during a rotation, causing inflow distortion or impingement noise, respectively. Non-uniform inflow usually results in increased noise intensity at higher BPF harmonics as well as inter-harmonic humps, while turbulence impingement results in a low-frequency broadband contribution. Steady loading noise is typically mitigated by uneven blade spacing (Duncan and Dawson 1974), while reducing unsteady loading or impingement noise is more challenging due to the involved complex flow physics.

One of the most documented flow non-uniformities, causing unsteady loading noise, is tip clearance noise, generated by coherent vortex structures present in the tip-gap region (Zhu et al. 2018) that interact with the blade tip and generate subharmonic humps (Marsan et al. 2018) in the far-field acoustic spectrum. Tip clearance noise is usually mitigated by applying a forward sweep to the blade geometry (Ghodake et al. 2022), installing a bell-mouth inlet (Kohout and Hyhlík 2020; Benedek et al. 2022), or adopting casing treatments (Zhu and Carolus 2018). Alternative approaches include introducing a rotating (Feng et al. 2023) or stationary (Piellard et al. 2014) ring that connects the blade tips and prevents the formation and growth of rotating coherent structures. It is worth noting that a rotating ring is commonly used in industrial applications, also to enhance the structural properties of blades by changing their stresses from tensile to compressive. Feng et al. (2023) showed that a rotating ring can reduce noise levels by mitigating tip leakage flow. Nevertheless, when the fan operates with a non-zero pressure rise, the presence of the ring can lead to upstream backflow, where interaction with the rotor blades increases

unsteady loading noise. Magne et al. (2015) found that blade-backflow interaction due to pressure rises is a major source of unsteady loading noise, while Bellelli et al. (2025a) further demonstrated that the backflow dominates when the fan operates at its best efficiency point. Strategies such as tailored short ducts (Sun et al. 2023), porous leading edges (Teruna et al. 2022), or serrated bio-inspired designs (Liang et al. 2023) have been conceived to deal with this noise source, albeit they can increase high-frequency broadband noise as well as clashing with industrial feasibility.

Another significant rotating loading noise source in cooling fans is rotor-stator interaction noise (Tyler and Sofrin 1962). If rotor-stator axial spacing is less than one blade chord, the potential effect of the stator vanes on the blades dominates over the blades wake impingement on the vanes (Canepa et al. 2015). Moreover, geometrical inhomogeneities can increase tonal noise levels (Pestana et al. 2018) and give rise to azimuthal pressure modes that cannot be predicted with the well-known Tyler and Sofrin relation (Tyler and Sofrin 1962). Unevenly spacing the vanes with specific modulations, as done by Duncan and Dawson (1975) and Mellin and Sovran (1970), is a typical solution. A more general approach has been proposed by Cattanei et al. (2021), but limited to the steady loading noise produced by the rotor and, to the authors best knowledge, it has not yet been applied to the stator vanes uneven spacing.

Despite extensive studies on noise reduction in engine cooling fans, significant gaps still persist. As a matter of fact, noise reduction technologies that mitigate backflow-rotor and non-viscous rotor-stator interaction noise sources have been rarely addressed, and optimization procedures to mitigate these effects are uncommon. Furthermore, a key issue is usually neglected: most noise reduction techniques are evaluated under simplified conditions on isolated fans rather than in more complex installation scenarios, such as configurations in the presence of a radiator. A previous study from the authors (Bellelli et al. 2026) pointed out how a radiator significantly impacts noise sources, with aeroacoustic performance being highly influenced by both the upstream non-uniform pressure loss, which alters the loading distribution on the blades, and the square-to-round shape transition between the casing and the fan responsible for additional recirculation upstream of the fan. These installation effects must be considered when comparing multiple fans on the same radiator (Sortor 2011) and, therefore, is expected to impact the efficacy of noise reduction techniques.

This paper investigates the impact of installation effects on two noise reduction strategies targeting different physical mechanisms in low-speed axial fans. Rotating ring shape modifications are considered to mitigate backflow-rotor interaction noise, which originates from unsteady loading induced by upstream recirculating flow structures. In contrast, uneven stator vane spacing is suggested to reduce rotor-stator interaction tonal noise associated with deterministic potential effects. Owing to their differ-

ent physical origins, these noise mechanisms are expected to depend differently on installation effects. The present work therefore, also evaluates how the presence of an upstream radiator, which alters the inflow non-uniformity and pressure distribution, differently impacts the effectiveness of these mitigation strategies under typical operating conditions. The results presented in this paper herein extend the findings reported in (Bellelli et al. 2025b), introducing an additional intermediate configuration in which only the rotating ring geometry is modified, while the stator vane azimuthal distribution is kept unchanged. This additional configuration allows the noise reduction associated with the ring shape modification to be clearly distinguished from the one provided by the optimized stator vane spacing. Furthermore, the analysis is extended through additional aerodynamic and acoustic investigations aimed at characterizing the dominant physical mechanisms responsible for noise generation and mitigation. In particular, the role of unsteady flow features and their impact on the acoustic footprint of the system are examined.

The rest of the paper is structured as follows: Section 2 describes the methodology used to calculate hydrodynamic and acoustic fields numerically. Section 3 describes the baseline and modified geometries as well as the radiator module. Section 4 describes the numerical setup used to perform the calculations. Section 5 discusses the results of the simulations, while the main conclusions are reported in Section 6. Appendix A summarizes the validation of the numerical simulations against the experiments and the mesh sensitivity study, already presented in previous works by the authors (Bellelli et al. 2025a; Bellelli et al. 2026).

2 Methodology

The flow field is computed through the commercial software 3DS PowerFLOW version 6, based on the Lattice-Boltzmann Method (LBM) (He and Luo 1997). Studies of low-speed fans for aeroacoustics of automotive products conducted with this solver are present in the literature (Ghodake et al. 2022; Sanjose et al. 2015; Perot et al. 2010; Pérot et al. 2013). When compared against numerical schemes based on the Navier-Stokes equations, the LBM shows lower numerical diffusion and dispersion. These considerations, along with its inherent compressibility, make the LBM particularly suited for aeroacoustics studies since only $10-15$ cells per wavelength are required to directly compute the acoustic field (He and Luo 1997).

The governing equation is the continuous Boltzmann equation

$$\frac{\partial f}{\partial t}+c_i\frac{\partial f}{\partial x_i}+\frac{F_i}{m_f}\frac{\partial f}{\partial c_i}=\mathscr{C}, \tag{1}$$

where $f(\vec{x},\vec{c},t)$ is the particle distribution function, namely the probability density of particles that have a microscopic velocity $\vec{c}$ at time t and position $\vec{x}$. $\vec{F}$ is the external force, m_f is the fluid molecular weight, and $\mathscr{C}$ is the collision operator, which models the variations in the distribution function caused by collisions between two particles. Since the collisions are elastic, the mass, momentum, and kinetic energy are conserved. As is common, the Bhatnagar, Gross, and Krook collision operator (Bhatnagar et al. 1954) is adopted, therefore

$$\mathscr{C} = -\frac{1}{\tau}(f - f^{eq}), \tag{2}$$

with τ the relaxation time and f^{eq} is the Maxwell-Boltzmann equilibrium distribution function, to which f tends to after the relaxation time τ has passed. It can be shown that the Navier-Stokes equations are recovered from Eq. 1 for low Mach numbers by performing a Chapman-Enskog expansion (Chapman and Cowling 1991).

Equation 1 is numerically discretized in space by dividing the computational domain into cubic lattices, called voxels, where particles can move only in a fixed number of directions. In its low Mach number solver version, adopted in this work, the model with 19 discrete velocity directions in three dimensions (Qian et al. 1992) is used. To consider the possibility of simulating rotating components, a sliding mesh approach is used (Zhang et al. 2011).

To properly capture the largest turbulent structures and, therefore, lower the computational cost, a Very Large Eddy Simulation (VLES) approach is employed by modifying the relaxation time as

$$\tau_{eff} = \tau + \tau_{turb}. \tag{3}$$

The sub-grid model is derived from the Renormalization Group $k-\varepsilon$ transport equations (RNG $k-\varepsilon$) (Chen et al. 2003). The Pressure-Gradient Extended Wall Model (PGE-WM) (Teixeira 1998), an extension of the generalized wall model proposed by Launder and Spalding (1983), is used.

In addition to the data directly provided by the solver, an additional analysis has been conducted to better describe the effects of the different noise reduction techniques and the influence of the radiator on their effectiveness. In particular, the mean acoustic contribution at a given virtual microphone of every surface of which the engine cooling module is composed has been computed through the *Opty∂B-pfnoisescan* (Casalino et al. 2021) tool. The resulting surface field is shown in frequency bands centered at the BPF and its first two harmonics as dB/m^2 and allows further localization of the regions of the solid surface that mainly contribute to the far-field noise. Such quantity can be interpreted as the noise contribution of each surface element at the considered probe in terms of acoustic pressure in the solid

formulation (Farassat and Succi 1982) of Ffwocs-Williams and Hawkings (FW-H) acoustic analogy.

3 Geometry

The present section describes the characteristic of the reference fan and radiator geometry, the noise reduction technologies implemented, and the test matrix of the numerical simulations. Both the fan and the radiator are industrial products, whose aerodynamic and acoustic performances have been previously numerically validated against experiments in the absence (Bellelli et al. 2025a) and in the presence (Bellelli et al. 2026) of the radiator. Nevertheless, a summary of validation against experiments and mesh sensitivity is reported in A.

The fan consists of a $D = 465$ mm diameter rotor with $B = 11$ unevenly spaced blades connected to a ring, a hub, a driving electrical motor, $N_v = 20$ unevenly spaced stator vanes, and a shroud, as shown in Fig. 1a. The fan tip clearance is equal to $0.01D$ and is shown in Fig. 1b. The blade chord at the tip is equal to $c/D = 0.14$. The fan is directly driven by the electric motor visible in Fig. 1a, without mechanical transmission or belt coupling to the engine. This configuration allows independent control of the fan rotational speed and improves the efficiency of the thermal management system. The fan driving motor is not a component being actively cooled and is included only to reproduce the physical configuration of the cooling module.

The radiator, of dimension $1.44D \times 1.48D$, is placed $0.02D$ upstream of the fan hub with a square casing that joins it to the fan, as shown in Fig. 2. The casing is joined to the fan shroud through 8 screws, covered by upstream protruding cylinders, as shown in the top left corner of Fig. 2. The radiator contains a water-glycol coolant mixture circulating inside the radiator tubes. Since the focus of this study is the aerodynamic and acoustic behavior of the fan, the internal coolant flow and the heat exchange between the air and the radiator are not explicitly simulated.

Throughout this paper, the automotive engine cooling fan shown in Fig. 1a without any radiator will be referred to as "isolated fan" (or "w/o Rad"). Conversely, the fan installed downstream of the radiator, as shown in Fig. 2, will be referred to as "full cooling module" (or "w/ Rad").

A previous study by the authors (Bellelli et al. 2025a) highlighted that a primary source of broadband noise, when the fan operates at maximum efficiency, is the interaction of the backflow, due to the pressure rise, with the blades leading edge in the near tip region ($r/R_{tip} \geq 0.8$). Therefore, a first modification of the fan geometry regarded the rotating ring shape. In Fig. 3 are reported sketches of the baseline ring (BSL Ring) (Fig. 3a) and the proposed low noise ring (LN Ring) geometry (Fig. 3b). The LN Ring is designed to redirect the backflow towards the radial direction and therefore prevent its interaction with

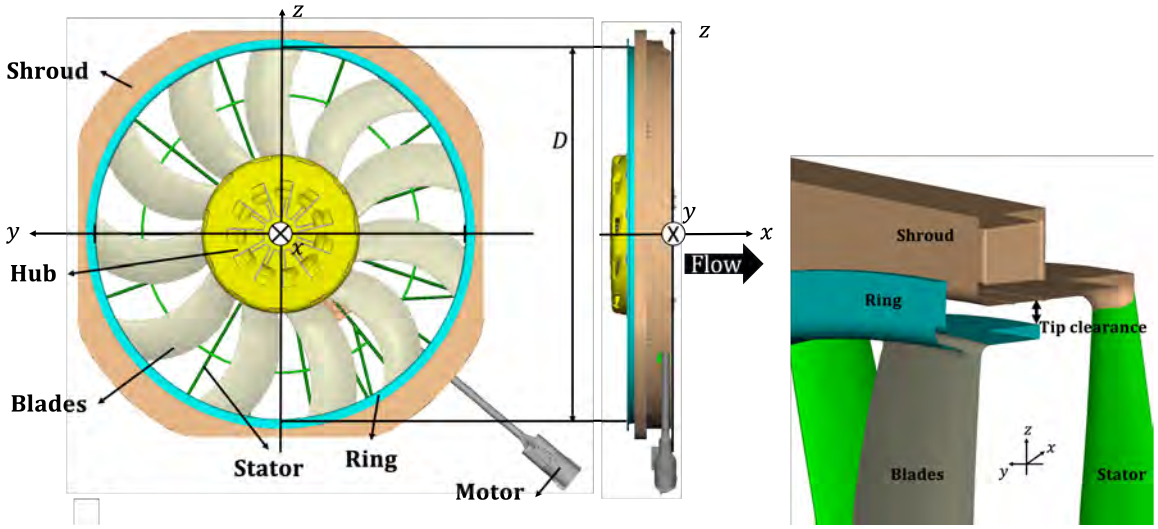

(a) (b)

Figure 1: Tested automotive engine cooling fan. The main parts in which the fan consists are shown with different colors. (a): Cooling fan. (b): Tip clearance detail.

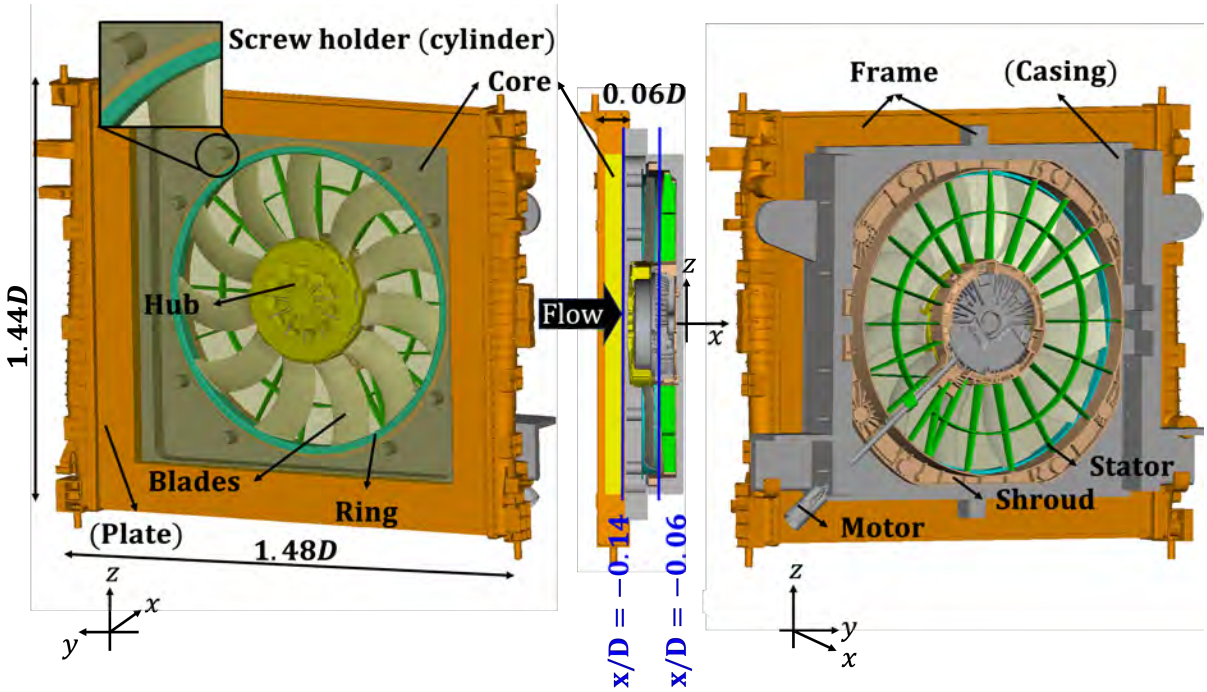

Figure 2: Tested cooling module. The radiator is shown in orange (solid part) and yellow (coolant tubes part, simulated as porous medium) while the square casing is shown in grey. The upstream ($x/D = -0.14$) and downstream($x/D = -0.06$) planes, where the averaged flow field will be shown, are highlighted in blue.

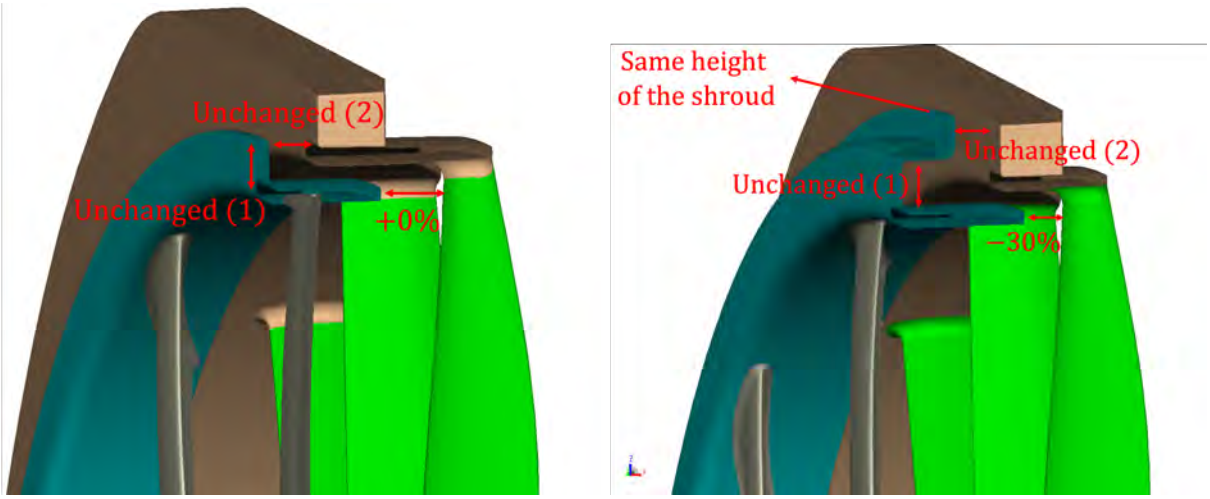

(a) (b)

Figure 3: Baseline and proposed low noise ring geometries. (a): Baseline. (b): Low noise.

the blades. This is obtained by adding a surface of revolution in the ring parallel to the x-axis so that the axial spacing between the ring and the shroud is kept constant, and an additional appendix to the ring in the radial direction so that the ring has the same height of the shroud on the $y = 0$ and $z = 0$ planes. The axial clearance between the ring and stator vanes is reduced by 30% to further accelerate the flow in the tip clearance, enhancing the flow radial redirection. The design has been realized following the manufacturer suggestions, considering manufacturing constraints.

The same study in (Bellelli et al. 2025a) showed that, for engine cooling fans characterized by narrow axial spacing between rotor and stator, rotor-stator potential (i.e. non viscous) interaction is a dominant source of tonal noise, especially at the BPF harmonics. It is therefore expected that an optimized spacing in the stator vanes azimuthal distribution can reduce rotor tonal noise by distributing the energy along several modes in the acoustic pressure spectrum. For this purpose, the second proposed modification to the fan geometry concerned the stator vanes azimuthal distribution. To optimize the stator vanes azimuthal distribution, an approach similar to the one described in (Cattanei et al. 2021) is used. Using the so-called interference function at each frequency of interest $f = n\Omega$

$$F_{int}(n) = \sum_{k=1}^{B} \exp(-in\alpha_k), \tag{4}$$

where i is the imaginary unit and α is the azimuthal position of the k-th blade, Cattanei et al. (2021) defined a useful metric to quantify the steady loading tonal noise of the rotor, namely the logarithmic excess

$$E = \sum_{n=1}^{M_h} 20\log_{10}\left\{\max\left[\frac{F_{int}(n)}{BF_{min}}, 1\right]\right\}, \tag{5}$$

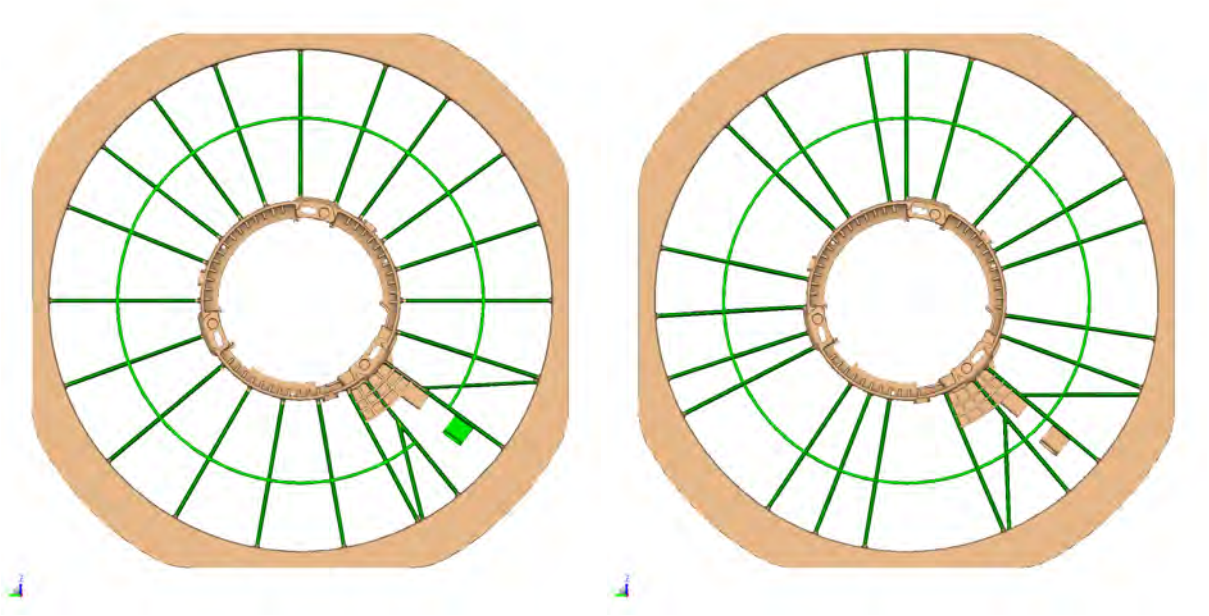

(a) (b)

Figure 4: Stator vanes azimuthal distribution. (a): Baseline. (b): Low noise.

where M_h is the maximum desired harmonic of the fan rotational frequency Ω (i.e., $f_{max} = M_h\Omega$) and F_{min} is an arbitrary threshold value for the interference function to be considered in the calculation. In this work, the interference function in Eq. 4 is used to describe the unsteady loading spectrum of each rotor blade due to the interaction with the potential field induced by the downstream stator vanes. By doing so, the same metric of Eq. 5 quantifies the rotor-stator potential interaction tonal noise on the rotor. Hence, an evolutionary optimization genetic algorithm (Lambora et al. 2019) is used to optimize the vanes angular positions through the minimization of the logarithmic excess in Eq. 5. Fig. 4 shows the baseline (BSL Vanes) and low noise (LN Vanes) stator vanes azimuthal distributions, the latter obtained with the aforementioned optimization procedure.

Both the ring and vanes modifications have been conceived assuming that they do not affect both the flow rate through the fan and the thrust on the fan disk for a fixed fan rotational speed (i.e., the operating point does not change). Nevertheless, the validity of this hypothesis for both modifications will be assessed through the course of the present work.

The isolated fan has been numerically tested in its baseline configuration (BSL Ring/BSL Stator, abbreviated to BSL for the sake of conciseness), with the low noise ring and baseline stator (LN Ring/BSL Stator), and with both low noise ring and low noise stator (LN Ring/LN Stator). On the contrary, in the full cooling module configuration, the system has been numerically tested only in its baseline (BSL Ring/BSL Stator) and full low noise (LN Ring/LN Stator) configurations since it is expected that the presence of the radiator will not substantially affect the rotor-stator potential interaction mechanism. When

	Isolated fan	**Full cooling module**
BSL Ring/BSL Stator	✓	✓
LN Ring/BSL Stator	✓	×
BSL Ring/LN Stator	×	×
LN Ring/LN Stator	✓	✓

Table 1: Summary of the numerically tested configurations.

the low noise configuration is tested on the full cooling module, the 8 cylindrical screw holders have been removed from the square casing as they have been shown to produce additional loading unsteadiness that is radiated in the far-field as tonal noise at a specific frequency ($f/BPF = 8/11$) and its harmonics, as already shown in (Bellelli et al. 2026). A summary of the numerically tested configurations is reported in Table 1.

4 Numerical setup

The computational domain used to simulate all the configurations is shown in Fig. 5. A large cubic fluid domain of side length equal to $135D$ is built to simulate a free-field environment. This side length size ensures that the distance between the acoustic sources and the outer boundaries is sufficiently large so that acoustic waves decay before reaching the domain boundaries and minimizes any reflection at the boundaries. Similar approaches and domain extents have been adopted in previous LBM aeroacoustic studies of axial fans (Sanjose et al. 2015; Pérot et al. 2013). The ceiling and the floor of the simulation domain are modeled as solid reflecting walls, while both the inlet and the outlet have a static pressure boundary condition. A discretization strategy based on 11 Variable Resolution (VR) regions is adopted; the voxel size between one VR region and the adjacent one is doubled. Each color of the scale in Fig. 5 represents a different VR region, where a higher value of VR is associated with a higher mesh resolution (i.e., smaller voxel size). As shown in Fig. 5, the regions with the highest resolutions are set around the rotating blades and near the tip gap region, where there are 11 voxels in the tip clearance. The resolution in the tip gap region is similar to the one adopted by Avallone et al. (2020). A sponge region is defined by an artificial change of viscosity of a factor of 100, with an exponential function between $8.6D$ (Sponge inner) and $12.9D$ (Sponge outer), as outlined in Fig. 5. Both the increase in voxel size and the sponge region are used to mitigate reflections of acoustic waves at the domain boundaries.

In the isolated fan configuration, a wall separating the two environments is modeled as a solid anechoic wall, as shown in Fig. 5. This ensured that a pressure rise across the fan can be imposed by initializing the upstream ambient with a lower pressure that matches the maximum efficiency point of the fan system. The resulting load coefficient is equal to $\psi = 0.1$, which corresponds to a flow coefficient

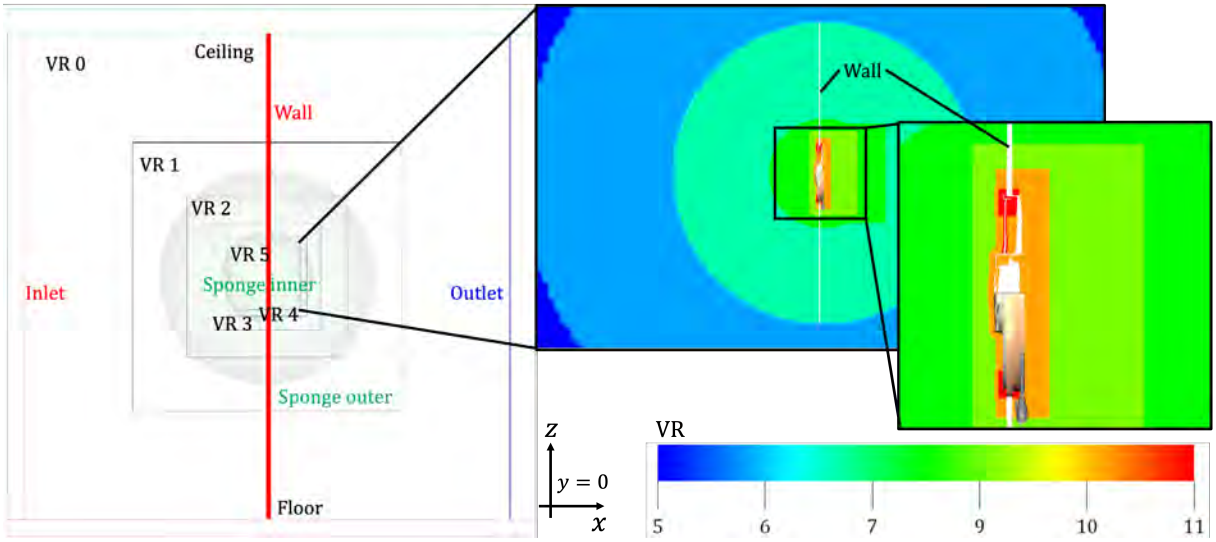

Figure 5: Sketch of the computational domain in the plane at $y/D = 0$.

equal to $\varphi = 0.14$ at a rotational speed $\Omega = 2868$ RPM.

In the full cooling module configuration, the radiator is modeled as an equivalent porous medium (Piellard et al. 2014). The radiator characteristic curve has been measured by the manufacturer in an aerodynamic testing facility certified according to the AMCA 210-99 standard and modeled through Darcy's law (Whitaker 1986). Unlike the isolated fan configuration, no bulk pressure rise is imposed in this configuration, as the equivalent porous medium provides the fan with a pressure loss. The resulting load coefficient is equal to $\psi = 0.07$, which corresponds to a flow coefficient equal to $\varphi = 0.13$ at a rotational speed $\Omega = 3048$ RPM. This ensured that both the isolated fan and the full cooling module configurations operate at their best efficiency point.

Simulations have been performed at a resolution equal to 1200 vox/D in the finest VR region for a physical time of 20 revolutions, while data are saved during the last 10 revolutions. The corresponding time-step is $\Delta t \approx 10^{-5}$ s, while the surface y^+ is below 60. In previous studies the authors have validated the numerical setup described here and assessed that the 1200 vox/D resolution reached mesh independence on both the isolated fan (Bellelli et al. 2025a) and full cooling module (Bellelli et al. 2026) configurations. For this reason, it is considered not necessary to perform again the validation and mesh convergence studies in the present work again. The results of the mesh independence study are summarized in A.

Pressure and velocity are sampled at 48 kHz on two perpendicular planes located respectively at $y/D = 0$ and $z/D = 0$. Three planes parallel to the fan are sampled at 3000 Hz; they are located at $x/D = -0.12$, $x/D = -0.06$, and $x/D = 0$, and are used to compute phase-locked flow fields. The three locations correspond respectively to the rotating ring upstream boundary, the rotor-stator interstage, and

the stator vanes trailing edge. Moreover, a small volume around the fan module is sampled at a frequency of 755 Hz and used to generate instantaneous flow field visualizations. All the solid surfaces of the cooling module are sampled at a frequency of 48 kHz. Integral values of blade loading, torque, and mass flow rate are sampled as well. The mass flow is sampled with a frequency of 48 kHz in a plane located at $x/D = 0$.

A fully circular array of 12 equally spaced far-field probes, located in the plane $z/D = 0$ at a radius $r/D = 2.15$ far from the fan center, is used to sample the acoustic field directly from the simulations and perform directivity analyses. In the experiments, only one probe located at $x/D = -2.15$, $y/D = 0$, and $z/D = 0$ is used, as is typical in industry. The spectral content of the probe signals $\tilde{p}$ is computed through the Welch averaging algorithm (Welch 1967) with 8 Hamming windows and 50% of overlap, resulting in a frequency resolution of 11.8 Hz. The acoustic performance is evaluated in terms of Sound Pressure Level (SPL) at each frequency resulting from the aforementioned spectral processing as

$$SPL = 20\log_{10}\left(\frac{\tilde{p}}{p_{ref}}\right), \tag{6}$$

where $p_{ref} = 20\,\mu$Pa is the commonly adopted reference acoustic pressure.

5 Results and discussion

The flow field is described in detail to characterize the aerodynamic mechanisms. The analysis includes visualization of coherent vortical structures, mean velocity and vorticity fields, spanwise velocity profiles, spectral analyses of velocity spatial fluctuations, and spectral analyses of loading temporal fluctuations. Vortical structures are identified using the Λ_2 vortex identification criterion (Jeong and Hussain 1995), which represents an alternative to the commonly used Q-criterion. Since both Q- and Λ_2-criterion identify regions where rotation dominates over strain, the qualitative identification of the vortical structures relevant to the present analysis is not affected by this choice.

The acoustic field is also investigated to assess the effectiveness of the noise reduction strategies under the studied conditions. The analysis includes spectral decomposition of pressure fluctuations, surface noise source localization, and directivity patterns of the radiated sound.

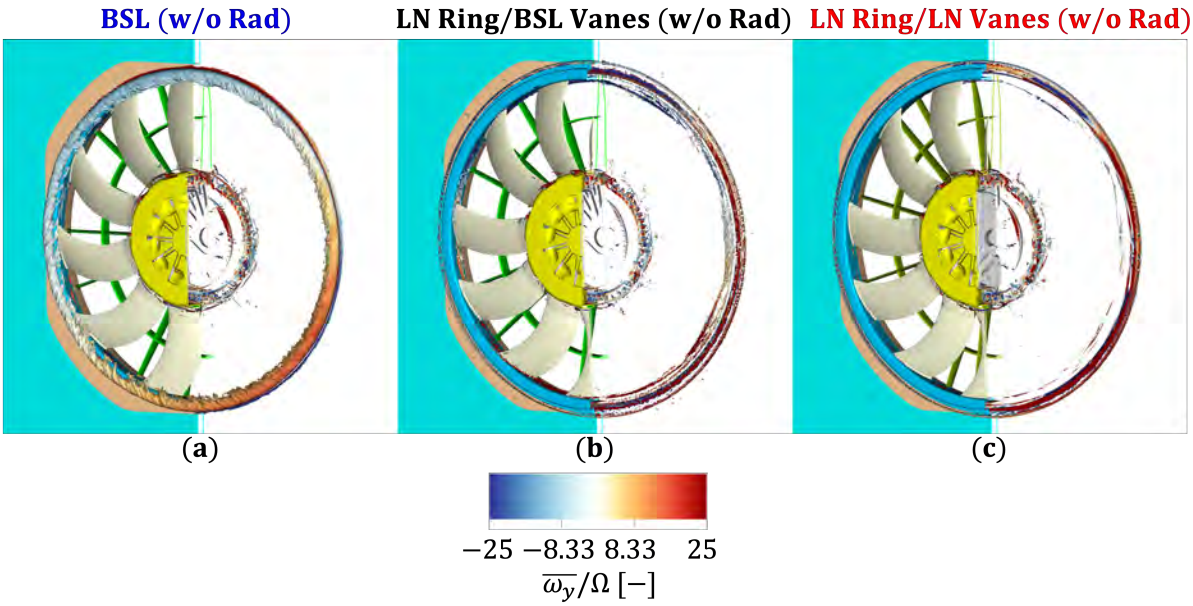

Figure 6: Mean $\Lambda_2/\Omega = -20$ iso-surfaces colored with the time-averaged y component of the vorticity at $x/D \leq -0.06$ on the isolated fan configuration. (a): BSL Fan/BSL Vanes. (b): LN Ring/BSL Vanes. (c): LN Ring/LN Vanes.

5.1 Isolated fan

5.1.1 Aerodynamic results

In Fig. 6, a three-dimensional visualization of the mean flow field for the isolated fan configuration is provided. The $\Lambda_2/\Omega = -20$ iso-surfaces colored with dimensionless y component of the time-averaged vorticity $\bar{\omega}/\Omega$ are shown at $x/D \leq -0.06$. The BSL configuration (Fig. 6a) is characterized by the presence of a strongly coherent vortex structure near the rotating ring, which clearly indicates the presence of a backflow. This is further confirmed by the vorticity value, which indicates that the vortex structure wraps around the ring. On the other hand, both LN Ring configurations (Figs. 6b and 6c) reveal that the backflow is mitigated, and almost no vortical structure is seen to wrap around the ring. As a matter of fact, vortices are concentrated into the tip clearance, and then they are convected in the radial direction without interacting with the rotor.

To better clarify these aspects, Fig. 7 shows the time-averaged y component of the dimensionless vorticity at $y/D = 0$, while Fig. 8 shows, in the same plane, the time-averaged dimensionless axial velocity component. In both figures, streamlines are superimposed. The backflow present in the BSL configuration (Figs. 8a and 8a) is visible as a region with high $\bar{\omega}_y$ absolute value. At this location, the backflow vortical structure firstly leaves the tip gap with a highly positive y-vorticity and then impacts the rotating ring area with a highly negative y-vorticity. This is in line with the findings reported in (Bellelli et al. 2025a). On the other hand, the LN Ring configurations (Figs. 7b-c and 8b-c) show a highly positive

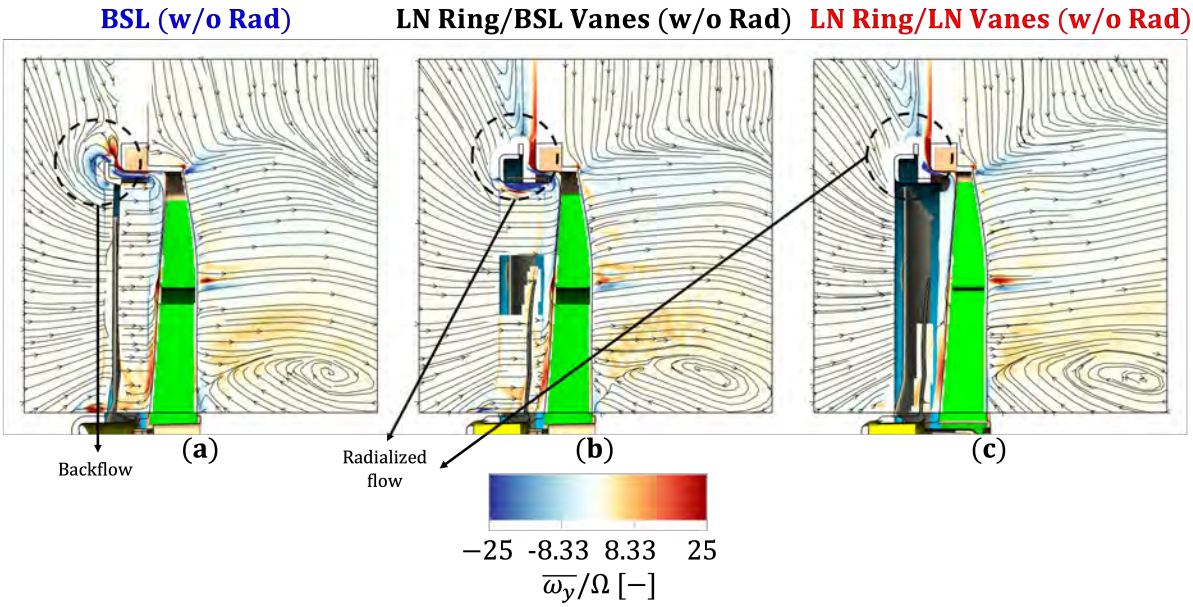

Figure 7: Time-averaged y component of the vorticity in a plane located at $y/D = 0$ on the isolated fan configuration. (a): BSL Fan/BSL Vanes. (b): LN Ring/BSL Vanes. (c): LN Ring/LN Vanes.

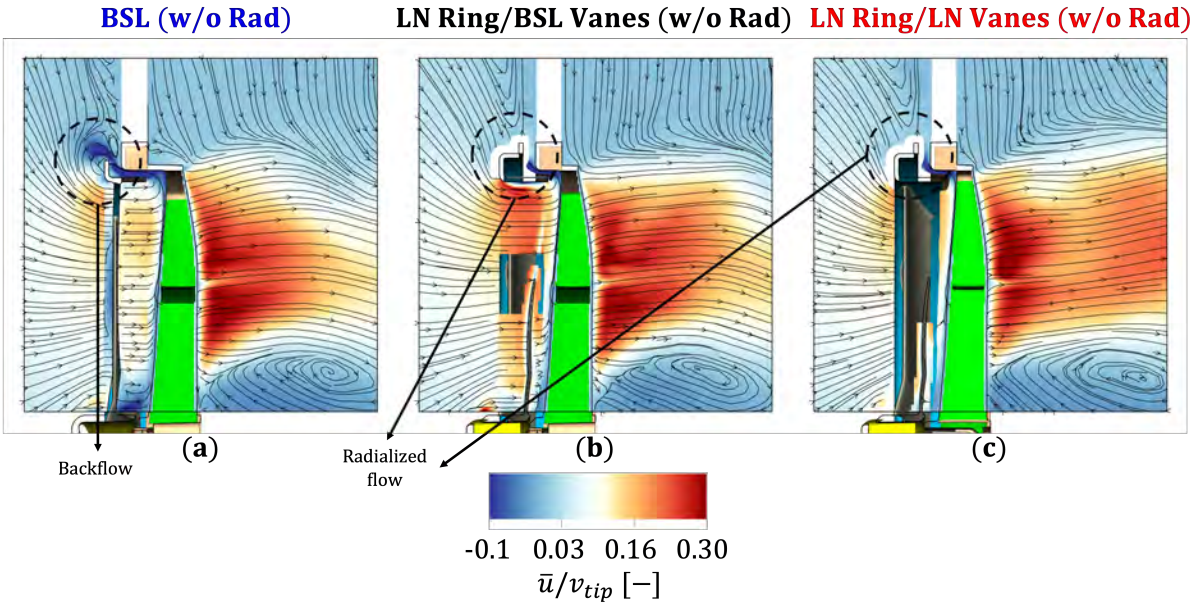

Figure 8: Time-averaged axial velocity in a plane located at $y/D = 0$ on the isolated fan configuration. (a): BSL Fan/BSL Vanes. (b): LN Ring/BSL Vanes. (c): LN Ring/LN Vanes.

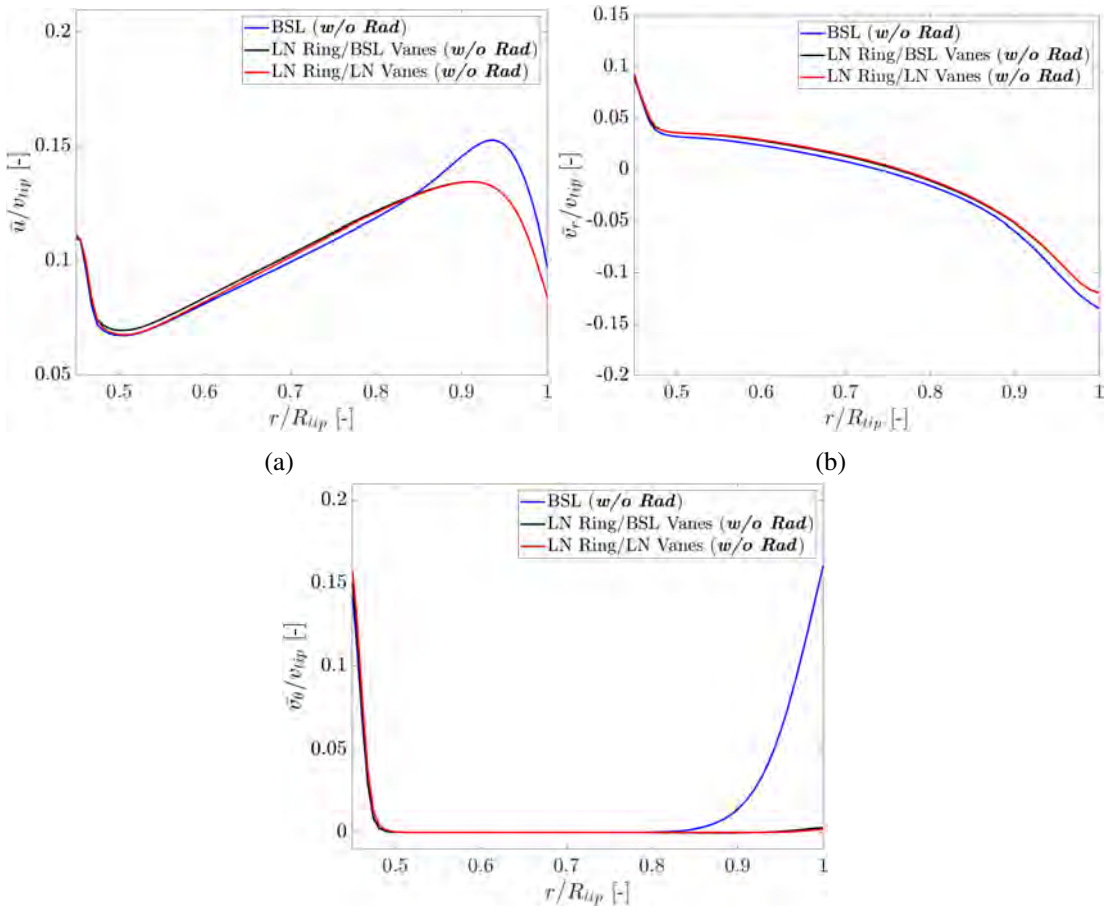

Figure 9: Time and azimuthally averaged velocity spanwise profiles upstream of the fan ($x/D = -0.14$) on the isolated fan configuration. (a): Axial velocity. (b): Radial velocity. (c): Tangential velocity.

y-vorticity region close to the thin wall, indicating that vortical structures are convected far from the fan, in the radial direction. This is better visualized by the streamlines above the tip, near the thin wall and further confirmed by the absence of the negative axial velocity region at the tip in Figs. 8b and 8c.

Fig. 9 shows the axial (Fig. 9a), radial (Fig. 9b), and tangential (Fig. 9c) velocity radial profiles at $x/D = -0.14$. The quantities have been azimuthally averaged over the whole fan disk. The LN Vanes do not particularly affect the velocity field upstream. Conversely, the LN Ring causes relevant differences in the near tip region ($r/R_{tip} \geq 0.8$). As a matter of fact, the axial velocity gradient (Fig. 9a) is substantially reduced, and the tangential velocity overshoot (Fig. 9c) is almost flattened. No particular impact is seen on the radial velocity (Fig. 9b) instead. These considerations confirm that the LN Ring successfully mitigates the backflow in the fan disk area by radially redirecting it.

To assess the azimuthal uniformity of the backflow and the impact of the noise reduction technologies, the axial velocity standard deviation contours at $x/D = -0.14$ are analyzed in Fig. 10. The BSL configuration (Fig. 10a) is characterized by high levels of axial velocity standard deviation near the tip

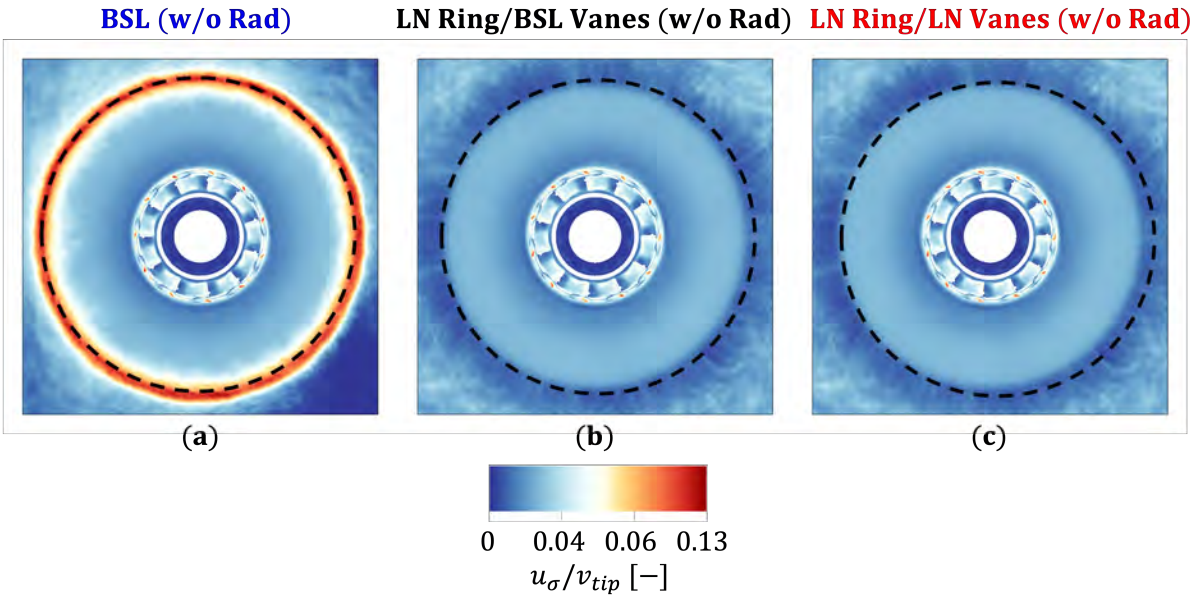

Figure 10: Axial velocity standard deviation in a plane located at upstream of the fan ($x/D = -0.14$) on the isolated fan configuration. (a): BSL Fan/BSL Vanes. (b): LN Ring/BSL Vanes. (c): LN Ring/LN Vanes.

because of the backflow, while the LN Ring configurations (Figs. 10b and 10c) show a reduction in the tip region, confirming that the modification in the ring shape can be considered successful on the isolated fan. It should also be noted the absence of any difference between the LN Ring/BSL Vanes (Fig. 10b) and the LN Ring/LN Vanes (Fig. 10c) configurations, confirming that the vanes azimuthal spacing does not affect the fluctuations in the upstream flow field.

Furthermore, the axial velocity standard deviation is analyzed in the frequency domain to quantitatively assess the mitigation of the unsteady component provided by the LN Ring. The azimuthal mode decomposition of the standard deviation of the axial velocity component is reported in Fig. 11. The quantity has been sampled on a circular line of radius $r/R_{tip} = 0.9$ at $x/D = -0.14$, sketched in Fig. 10. The frequency has been made dimensionless with the BPF, while the velocity has been made dimensionless with the tip velocity. As expected, the broadband content in the low noise configurations is lower, meaning that the axial velocity fluctuations upstream of the fan have been cut down by the LN Ring. Similar findings are obtained when the LN Vanes are added.

The impact of the LN Vanes on the potential flow field in the rotor-stator interstage is quantified with a similar analysis. Fig. 12 shows the spatial Fourier transform of the mean axial velocity sampled on a circular line of radius $r/R_{tip} = 0.75$ at $x/D = -0.06$. The quantity has been sampled in the fixed reference frame so that the rotor wake could be averaged out, thus leaving only the potential field produced by the stator vanes. It can be observed that the LN Ring does not sensibly contribute to redistributing the energy among the different modes, while the LN Vanes configuration shows a more broadband distribution. This

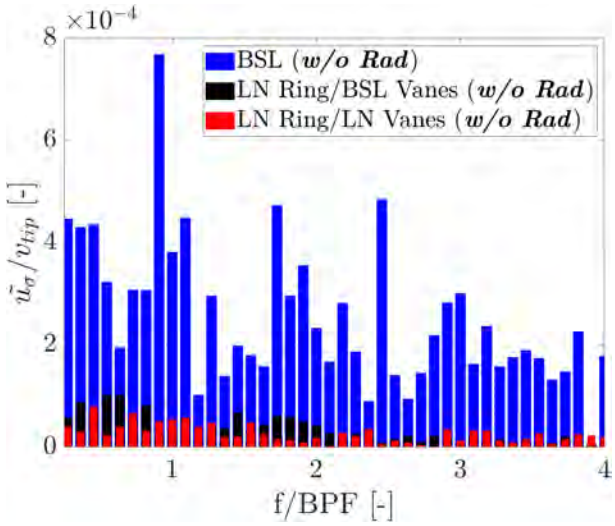

Figure 11: Azimuthal mode decomposition of the axial velocity component standard deviation sampled on a fully circular line at $r/R_{tip} = 0.9$ in a plane located upstream of the fan ($x/D = -0.14$) on the isolated fan configuration.

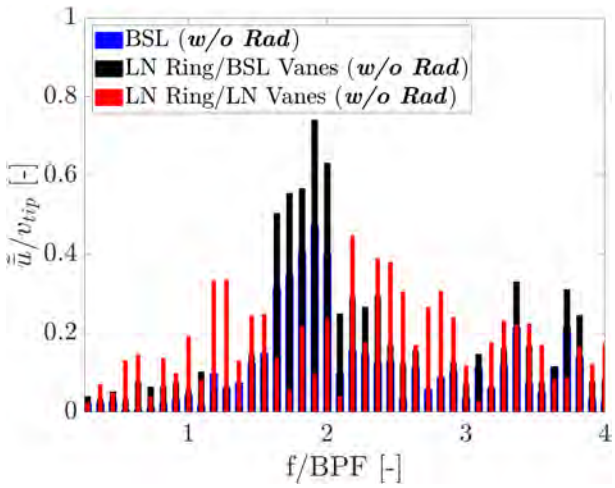

Figure 12: Azimuthal mode decomposition of the mean axial velocity component sampled on a fully circular line at $r/R_{tip} = 0.75$ in a plane located in the interstage between the rotor and the stator ($x/D = -0.06$) on the isolated fan configuration.

	ΔT	$\Delta \dot{V}$	ΔQ
BSL Ring/BSL Vanes	0%	0%	0%
LN Ring/BSL Vanes	-1%	+6%	+10.5%
LN Ring/LN Vanes	-2%	+7.5%	+11%

Table 2: Aerodynamic performance percentage variation with respect to the baseline configuration on the isolated fan configuration.

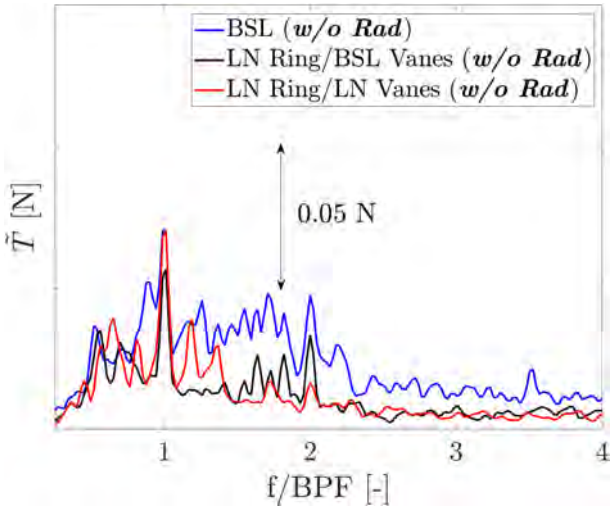

Figure 13: Spectrum of the rotor thrust on the isolated fan configuration.

means that the vane azimuthal distribution can be optimized with a very similar procedure to the one used to optimize the blades uneven spacing.

The impact of the noise reduction technologies on the aerodynamic performance of the isolated fan is analyzed. Table 2 shows the percentage variations of thrust, volume flow rate and torque of the LN Ring/BSL Vanes and LN Ring/LN Vanes configuration with respect to the baseline isolated fan. The quantities are obtained as an average over the last 10 revolutions. A decrease of 1% in thrust is seen as a result of both the LN Ring and LN Vanes; this can be considered to be negligible. On the other hand, the volume flow rate across the fan increases mostly because of the LN Ring, with an additional 1.5% given by the LN Vanes. This is a consequence of the fact that the backflow is successfully redirected by the LN Ring and interacts less with the rotor. Moreover, this means that the fan operating point is slightly changed with respect to the baseline configuration. This should be taken into account when optimizing the fan geometry. In addition, the LN Ring provides a substantial increase in torque that is associated with the increase in aerodynamic surface given by the LN Ring. It can be observed again that the LN Vanes does not affect much the torque (+0.5%). Therefore, it can be inferred that the LN Ring alters the aerodynamic performance of the isolated fan more than the LN Vanes.

To conclude the aerodynamic analysis of the isolated fan configuration, the spectrum of the rotor thrust is shown in Fig. 13, where the frequency has been made dimensionless with the BPF. It is seen

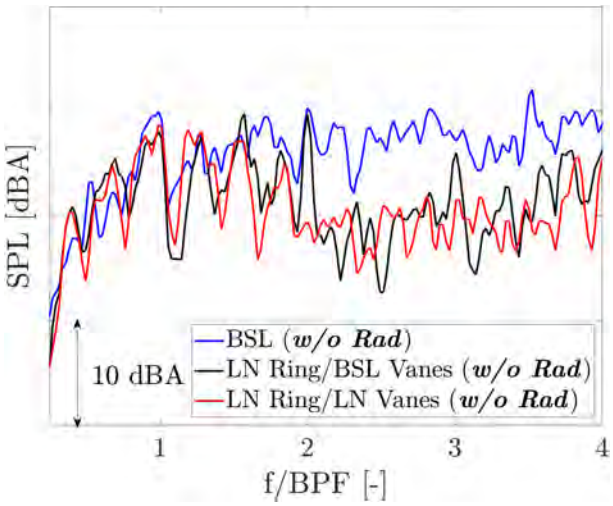

Figure 14: Pressure fluctuations at $x/D = -2.15$, $y/D = 0$, $z/D = 0$ (upstream, on the fan rotational axis) on the isolated fan configuration.

that the LN Ring significantly reduces the broadband content of the thrust spectrum since the backflow does not interact with the blades anymore. Moreover, it can be observed that the LN Vanes successfully decrease the first BPF harmonic peak, while slightly increasing the BPF peak that, however, remains unchanged with respect to the baseline configuration. Finally, the energy redistribution provided by the LN Vanes has the effect of increasing subharmonic frequencies in the range $0.5 \leq f/BPF \leq 1.5$.

5.1.2 Acoustic results

Fig. 14 shows the spectrum of the pressure fluctuations sampled along the fan rotational axis at $x/D = -2.15$, $y/D = 0$, and $z/D = 0$ as in a typical experimental setting. The plot confirms what is seen in the rotor thrust spectrum (Fig. 13), by showing a relevant broadband noise reduction provided by the LN Ring for $f/BPF \geq 2$ as well as a reduction (-10 dBA) of the first BPF harmonic peak. The BPF peak is reduced by about 1.5 dBA in both configurations. The OASPL computed in the frequency range $0 \leq f/BPF \leq 4$ is reduced by about 4 dBA with the LN Ring and by an additional 1 dBA by the LN Vanes.

Opty∂B-pfnoisescan is used to detect the time-averaged contribution of each surface element to the far-field noise in dB/m^2, at the same microphone position of Fig. 14. Two frequencies are analyzed: the BPF (Fig. 15a) and its first harmonic (Fig. 15b). In each row of the figure, both the front (left) and rear (right) views of the fan are reported for the three isolated fan configurations. A higher value of dB/m^2 in a certain part of the surface indicates a higher contribution of that part to the acoustic signal at the microphone of interest. At the BPF (Fig. 15a), the baseline configuration shows high intensity spots located in the tip region of the blade leading edge and on the rotating ring surface. Moreover,

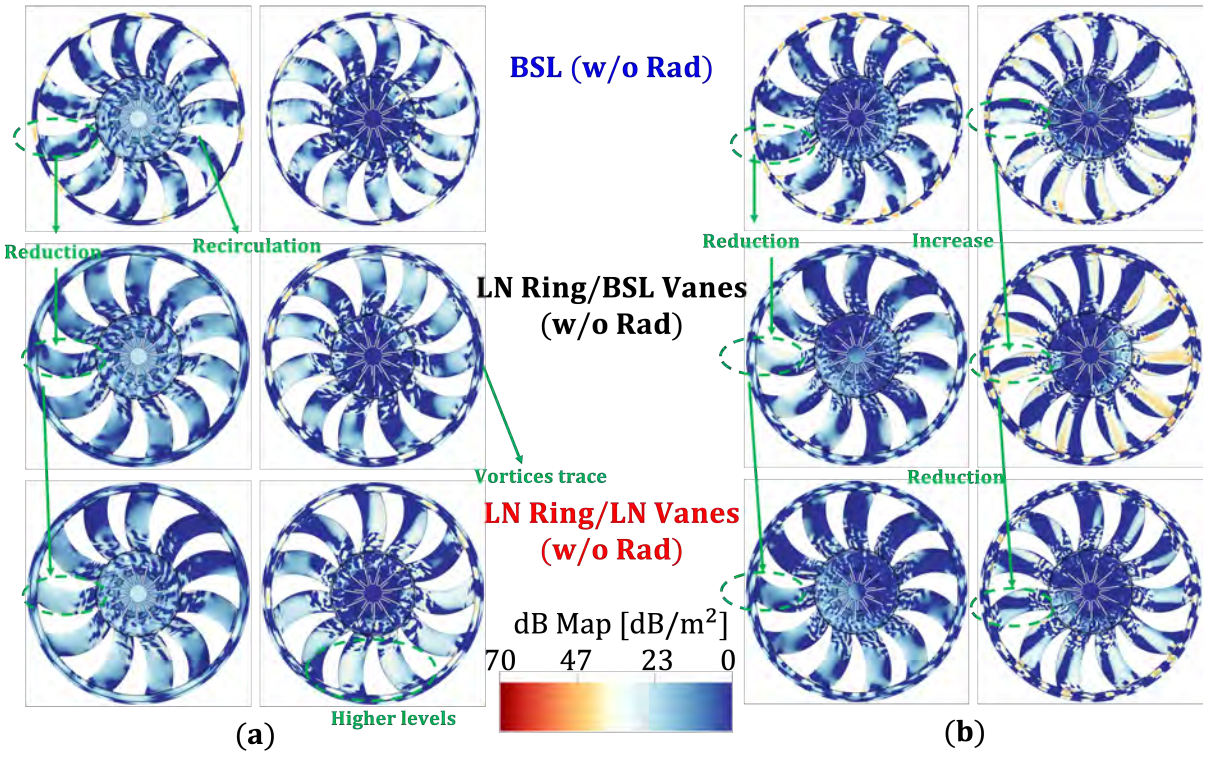

Figure 15: Surface noise contribution at the probe located at $x/D = -2.15$, $y/D = 0$, and $z/D = 0$ in the far-field on the isolated fan configuration. The bandwidth is $\Delta f/BPF = 0.18$. (a): Frequency centered at $f = BPF$. (b): Frequency centered at $f = 2BPF$.

the trace of flow recirculation at the hub is visible (Bellelli et al. 2026). Both the LN Ring and LN Vanes show a reduction in dB/m^2 at the tip, confirming that the broadband noise reduction seen in Fig. 14 is due to the backflow redirection that prevents it from interacting with the rotor. Furthermore, the LN Vanes show a slightly higher contribution in the rear side (right column), which suggests that the noise at the BPF is now dominated by rotor-stator potential interaction. At the first BPF harmonic (Fig. 15b), a lower intensity in the near tip region for the LN Ring/BSL Vanes with respect to the BSL configuration is observed. On the other hand, there are higher intensity spots in the rear side that are compatible with the rise of a narrowband peak at $f/BPF = 2$ pointed out in Fig. 14. When the LN Vanes are introduced, instead, the intensity levels on the rear side are reduced, confirming that the azimuthal spacing redistribution of the stator vanes mitigates the rotor-stator potential interaction noise contribution. Finally, the rear views of the fan at both the BPF and its first harmonic show the trace of vortex structures at the tip for all the tested geometries associated with flow separation phenomena at the tip (Bellelli et al. 2026).

The directivity patterns at the BPF and its first two harmonics, as well as on the overall SPL, in the frequency range $0 \leq f/BPF \leq 4$, are shown in Fig. 16. The plots show the SPL on a fully circular array of 12 probes located in the plane $z/D = 0$. It is seen that the LN Ring has a marginal impact on

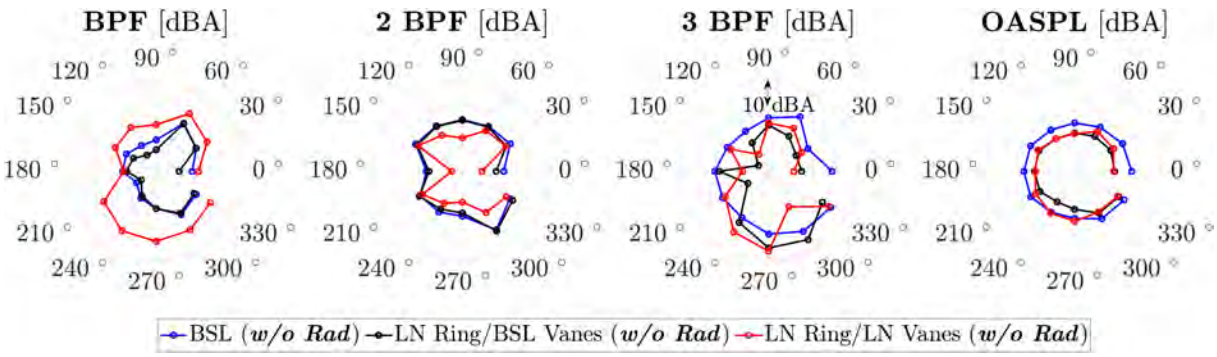

Figure 16: Directivity plots of the acoustic pressure at the BPF, the first two harmonics of the BPF, and the OASPL over the frequency range $0 \leq f/BPF \leq 4$ on the isolated fan configuration ($z/D = 0$).

the directivity of the BPF and of the first two harmonic tones, while the level reduction is more evident on the OASPL, which is reduced evenly on every probe. Furthermore, it is worth noting that the LN Vanes increase the SPL at the BPF in correspondence with the probes not aligned with the fan rotational axis. This is attributed to the increase of loading peaks near the BPF seen in Fig. 13. Indeed, these frequencies do not contribute to the noise on the fan rotational axis but to the noise at probes out of the fan rotational axis due to the radiation efficiency (Lowson 1970; Lowson 1965). Such a phenomenon is not seen; instead, at the first BPF harmonic, the noise is reduced almost evenly on every probe. At the second BPF harmonic, the directivity pattern is not substantially changed, while for the OASPL, the LN Vanes do not provide any sensitive difference with respect to the LN Ring.

5.2 Full cooling module

Since the individual contribution of the LN Vanes has already been analyzed in Sec. 5.1, only the BSL Fan/BSL Vanes and LN Ring/LN Vanes configurations are presented in the remainder of the paper.

5.2.1 Aerodynamic results

The $\Lambda_2/\Omega = -20$ iso-surfaces at $x/D \leq -0.06$ colored with dimensionless y component of the time-averaged vorticity $\bar{\omega}/\Omega$ are shown in Fig. 17. In this case, the BSL configuration (Fig. 17a) does not show visible coherent vortex structure upstream of the fan, as on the isolated fan (Fig. 6a), due to the lower pressure rise seen by the fan when placed in the full cooling module. Instead, coherent structures are located in the tip clearance and in correspondence with the cylinders in the casing (Bellelli et al. 2026). Differently, the LN Ring/LN Vanes configuration (Fig. 17b) reveals the presence of four coherent vortex structures at the centre of each casing side. They form because of the flow confinement caused by the casing. This means that the LN Ring/LN Vanes configuration installed downstream of the radiator is characterized by more vortical structures upstream of the fan caused by a stronger backflow interacting

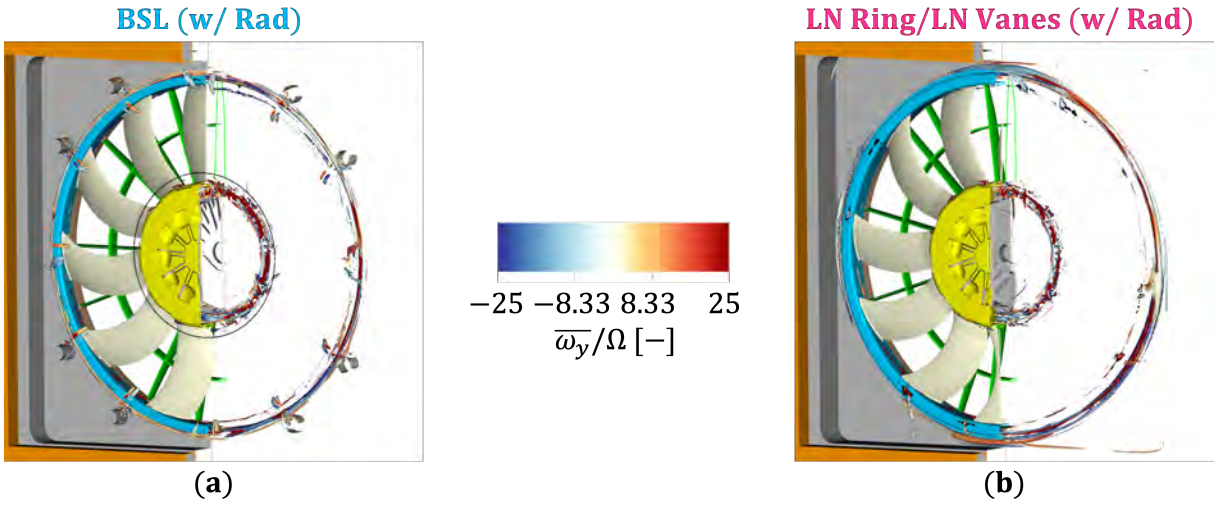

Figure 17: Mean $\Lambda_2/\Omega = -20$ iso-surfaces colored with the y component of the vorticity on the full cooling module configuration at $x/D \leq -0.06$. (a): BSL Fan/BSL Vanes. (b): LN Ring/LN Vanes.

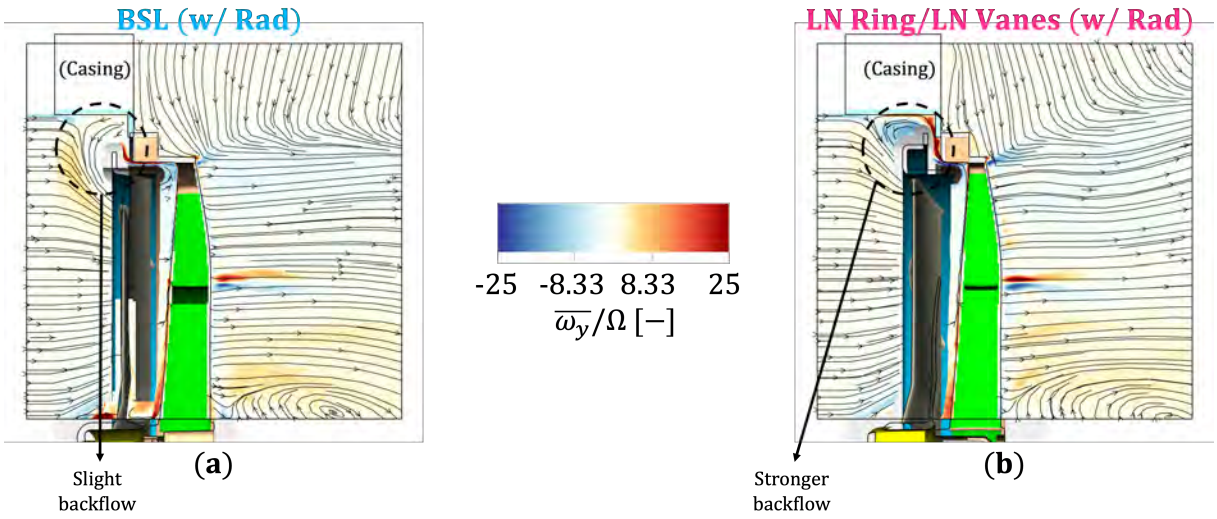

Figure 18: Time-averaged y component of the vorticity in a plane located at $y/D = 0$ on the full cooling module configuration. (a): BSL Fan/BSL Vanes. (b): LN Ring/LN Vanes.

with the rotor.

To clearly visualize this, Fig. 18 shows the time-averaged dimensionless vorticity y component at $y/D = 0$ while Fig. 19 shows the time-averaged dimensionless axial velocity in the same plane. In both figures, streamlines are superimposed. It is seen that the BSL configuration (Figs. 18a and 19a) is characterized by a less intense backflow with respect to the isolated fan configuration (Figs. 7a and 8a); this is in line with the lower pressure rise perceived by the fan in the full cooling module configuration. Moreover, Fig. 18a shows lower absolute values of y-vorticity compared to the isolated fan configuration (Fig. 7a). However, a slightly high y-vorticity spot is localized upstream of the rotating ring, highlighting that an additional large-scale vortex structure is coming from the radiator core; as suggested also by the

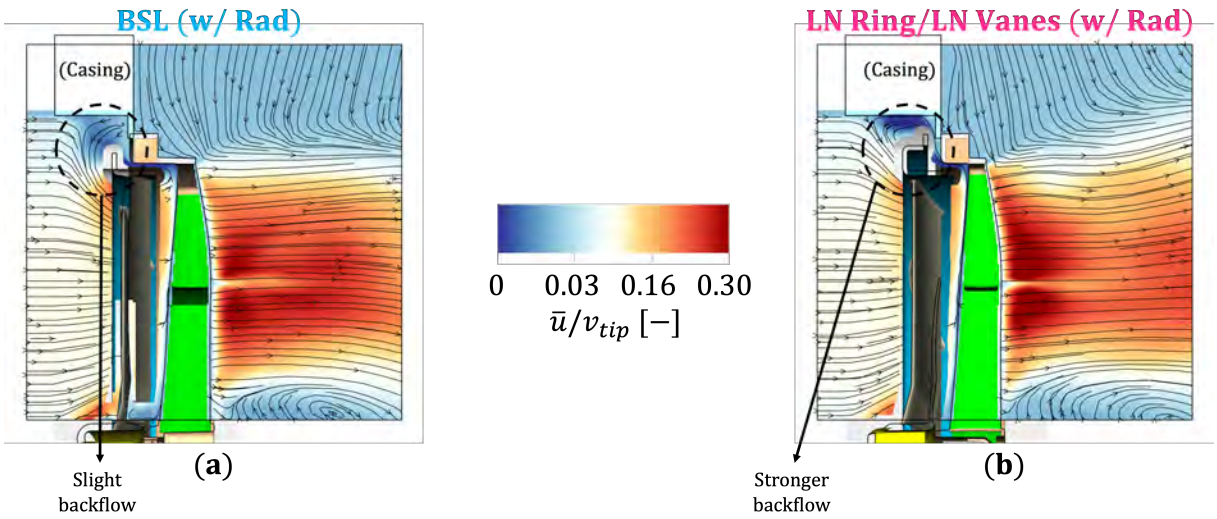

Figure 19: Time-averaged axial velocity in a plane located at $y/D = 0$ on the full cooling module configuration. (a): BSL Fan/BSL Vanes. (b): LN Ring/LN Vanes.

streamlines, the backflow and the large-scale vortex structure coming from the radiator core merge in the midpoint between the fan rotating ring and the radiator core plane. On the other hand, the LN Ring/LN Vanes configuration (Figs. 18b and 19b) reveals the presence of a stronger backflow compared to the BSL one, visualized either as a high negative axial velocity or as a high positive y-vorticity region in the tip gap. This occurs because the casing that joins the fan to the radiator acts as a flow confiner, preventing the backflow to be redirected towards the radial direction as in the isolated fan configuration. This is also visualised by the highly negative y-vorticity value in the rotating ring region. Therefore, the LN Ring shape does not mitigate the backflow in the presence of a flow confinement (i.e., the casing) as it fails to redirect the backflow towards the radial direction.

The time and azimuthally averaged flow field upstream of the fan is reported in Fig. 20, where the axial (Fig. 20a), radial (Fig. 20b), and tangential (Fig. 20c) velocity radial profiles at $x/D = -0.14$ are shown. Both the axial and radial velocity profiles are not substantially affected by the modifications to the vanes and rotating ring. If, on one hand, this is in line with Fig. 9 for what concerns the radial velocity, on the other hand, it is different in terms of axial velocity. Indeed, the axial velocity hump in the region $r/R_{tip} \geq 0.8$ is still present in the case of the low noise geometry in the full cooling module configuration. Moreover, Fig. 20c shows that the low noise geometry is characterized by a higher value of the tangential velocity component in the near tip region with respect to the baseline geometry. These considerations indicate that, unlike the isolated fan configuration, a backflow pattern is still present in the low noise geometry.

The azimuthal distribution of the unsteady flow field upstream of the fan is thereafter characterized in the following. Fig. 21 displays the contours of the standard deviation of the axial velocity in the

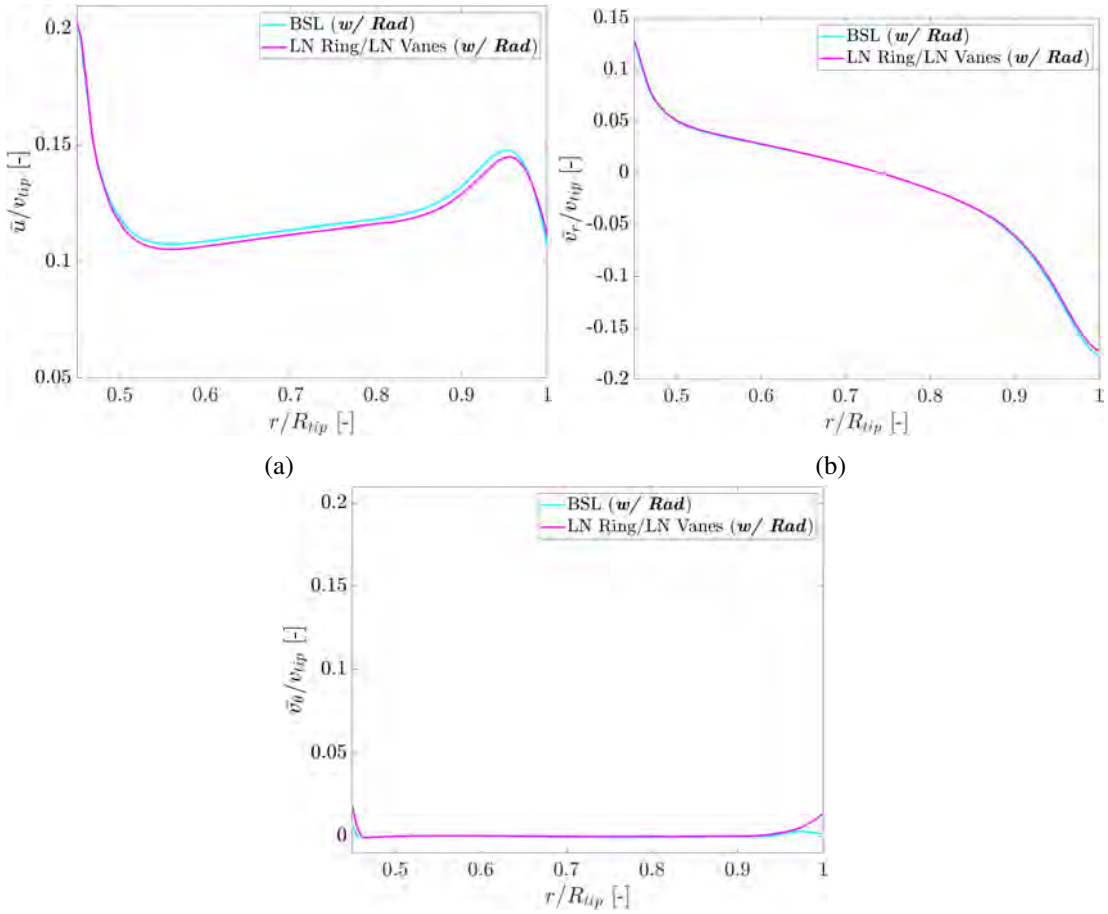

Figure 20: Time and azimuthally averaged velocity spanwise profiles upstream of the fan ($x/D = -0.14$) on the full cooling module configuration. (a): Axial velocity. (b): Radial velocity. (c): Tangential velocity.

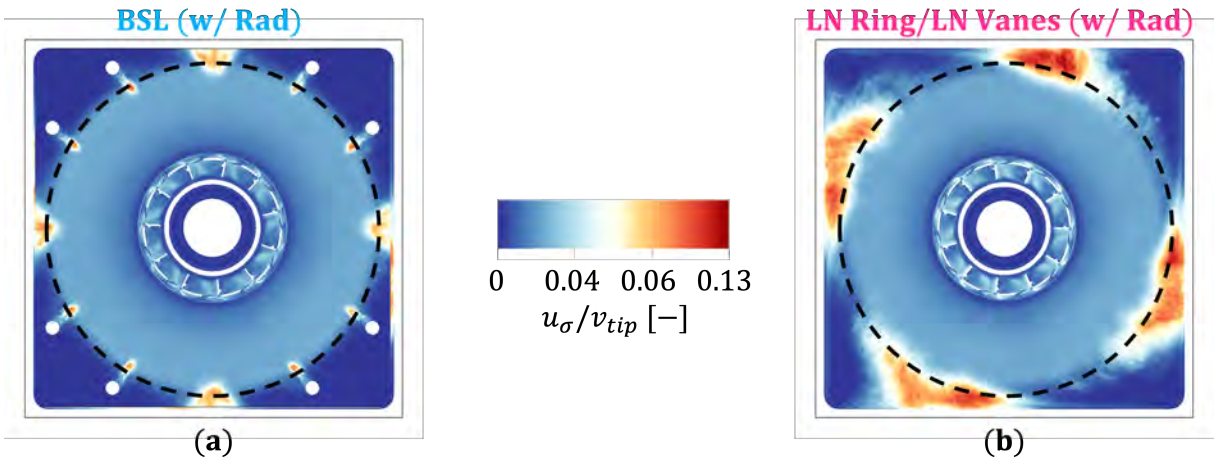

Figure 21: Axial velocity standard deviation in a plane located at upstream of the fan ($x/D = -0.14$) on the full cooling module configuration. (a): BSL Fan/BSL Vanes. (b): LN Ring/LN Vanes.

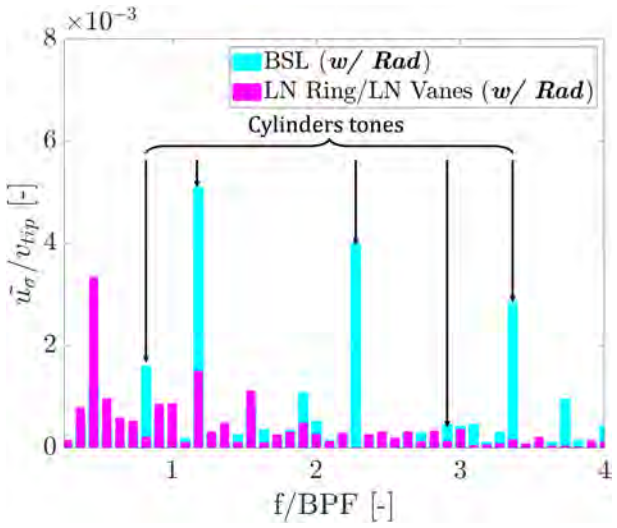

Figure 22: Azimuthal mode decomposition of the axial velocity component standard deviation sampled on a fully circular line at $r/R_{tip} = 0.9$ in a plane located in the interstage between the rotor and the stator ($x/D = -0.14$) on the full cooling module configuration.

plane at $x/D = -0.14$. The low noise configuration (Fig. 21b) shows higher fluctuation levels than the baseline one (Fig. 21a). This confirms that the presence of the square casing upstream of the fan prevents the backflow from being radially redirected due to the flow confinement. As a result, the axial velocity fluctuations are increased and concentrated in the regions of the casing where there is lower radial spacing between the casing and the fan. It is also observed that the absence of the cylinders wake in the low noise configuration (Fig. 21b) is because they were removed.

Fig. 22 shows the azimuthal mode decomposition of the standard deviation of the axial velocity sampled on the circular line of radius $r/R_{tip} = 0.9$ at $x/D = -0.14$, sketched in Fig. 21. The plot shows that the broadband content of the low noise geometry is only slightly reduced with respect to the baseline one, as the backflow is still present and interacts with the rotor. These considerations highlight that the presence of a radiator upstream not only affects the noise sources of the fan but also the effectiveness of noise reduction technologies acting on physical phenomena that are influenced by the radiator installation. Moreover, it can be observed that the tonal content at mode orders that are multiples of the number of cylinders (8) in the square casing is drastically reduced in the low noise geometry due to the absence of the cylinders. Only a prominent peak at $f/BPF = 4/11$ is left, which is a result of vortex structures concentrated at the center of each square casing side.

Fig. 23 shows the spatial Fourier transform of the mean axial velocity sampled on a circular line of radius $r/R_{tip} = 0.75$ at $x/D = -0.06$. The low noise geometry shows a broader energy spread among more modes, consistent with what is shown in Fig. 12 for the isolated fan configuration. This means that the vanes spacing is not much affected by the presence of a radiator located upstream, thus representing

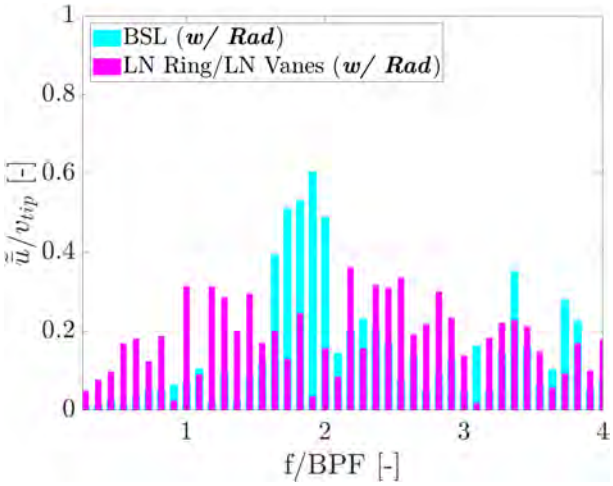

Figure 23: Azimuthal mode decomposition of the mean axial velocity component sampled on a fully circular line at $r/R_{tip} = 0.75$ in a plane located in the interstage between the rotor and the stator ($x/D = -0.06$) on the full cooling module configuration.

	ΔT	$\Delta \dot{V}$	ΔQ
BSL Ring/BSL Vanes	0%	0%	0%
LN Ring/LN Vanes	-0.5%	-2.5%	+2.5%

Table 3: Aerodynamic performance percentage variation with respect to the baseline configuration on the full cooling module configuration.

a viable noise reduction technology also in the presence of a more complex installation.

Percentage variations of thrust, volume flow rate and torque of the low noise (LN Ring/LN Vanes) geometry with respect to the baseline (BSL Ring/BSL Vanes) geometry on the full cooling module configuration are reported in Table 3. In the presence of the radiator, the quantities in Table 3 show less variation with respect to the isolated fan. More in detail, none of the quantities in Table 3 exceeds a variation of 2.5%. The thrust and torque respectively decrease and increase, consistently with what is shown in Table 2, albeit the torque increases by a smaller amount. In contrast to the isolated fan configuration, the volume flow rate decreases, indicating that the presence of the radiator alters the upstream flow field. Furthermore, the relatively small variation in volume flow rate indicates that the presence of the radiator reduces the fan sensitivity to changes in the operating point.

Fig. 24 shows the spectral content of the rotor thrust, which highlights how the broadband content increases for the low noise geometry, while the peak at the BPF is reduced. Furthermore, an increase in the peaks at frequencies near the BPF ($0.5 \leq f/BPF \leq 1.5$) is seen, consistently with what shown for the isolated fan configuration in Fig. 13. The reduction in amplitude due to the absence of the 8 cylinders seen in Fig. 22 is not seen in the thrust spectrum because the rotor-backflow interaction contribution dominates over the tonal one.

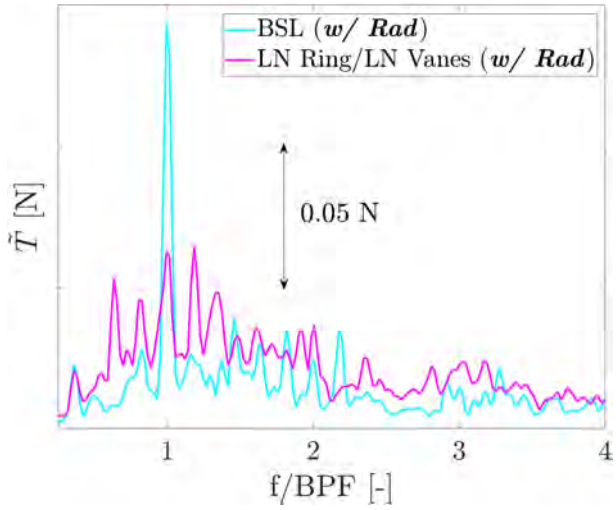

Figure 24: Spectrum of the rotor thrust on the full cooling module configuration.

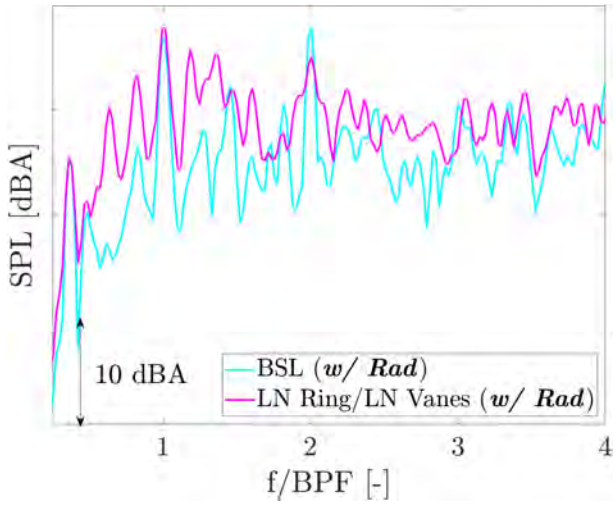

Figure 25: Pressure fluctuations at $x/D = -2.15$, $y/D = 0$, $z/D = 0$ (upstream, on the fan rotational axis) on the full cooling module configuration.

5.2.2 Acoustic results

The spectrum of the pressure fluctuations sampled at $x/D = -2.15$, $y/D = 0$, and $z/D = 0$ is shown in Fig. 25. As expected, the broadband content of the low noise geometry is increased with respect to the baseline one, as a result of the rotor-backflow interaction that the LN Ring is not able to mitigate in the presence of the radiator. On the other hand, the tonal content is reduced, although by a smaller amount with respect to the isolated fan configuration (Fig. 14) as a result of the LN Vanes. Quantitatively, the SPL at the BPF varies within 1 dBA, while the SPL at the first BPF harmonic is reduced by only 3 dBA. The OASPL in the frequency range $0 \leq f/BPF \leq 4$ is increased by 2 dBA as a result of the broadband noise increase.

Fig. 26 shows the surface noise contribution in dB/m^2 at the probe located at $x/D = -2.15$, $y/D = 0$,

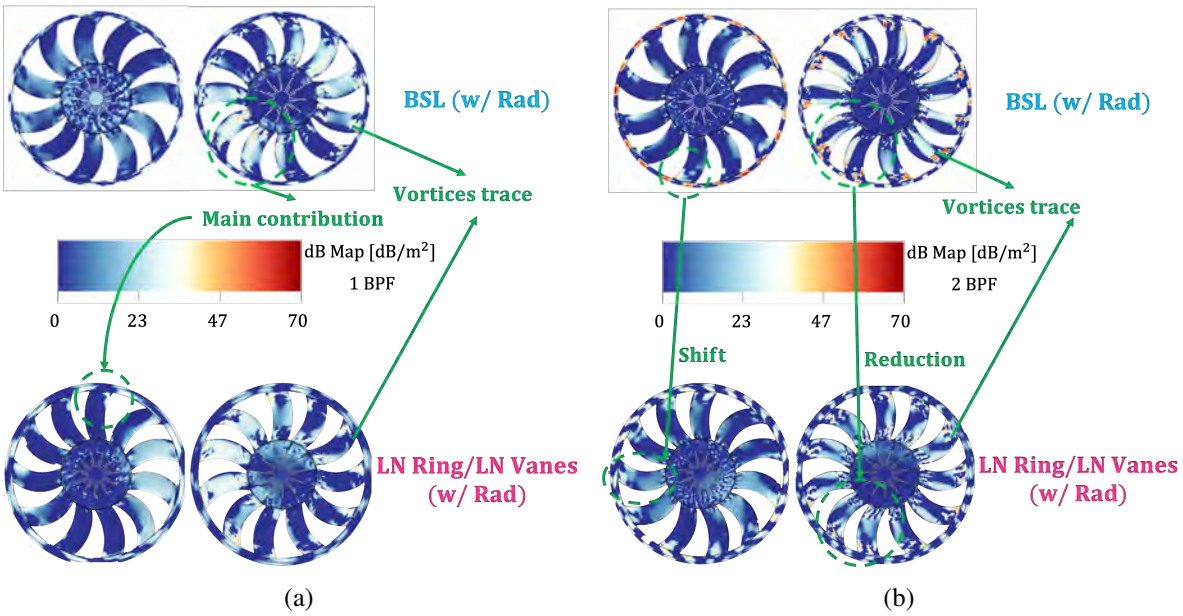

Figure 26: Surface noise contribution at the probe located at $x/D = -2.15$, $y/D = 0$, and $z/D = 0$ in the far-field on the full cooling module configuration. The bandwidth is $\Delta f/BPF = 0.18$. (a): Frequency centered at $f = BPF$. (b): Frequency centered at $f = 2BPF$.

and $z/D = 0$ in the far-field, centered at $f/BPF = 1$ (Fig. 26a) and at $f/BPF = 2$ (Fig. 26b) with a bandwidth of $\Delta f/BPF = 0.18$. At the BPF (Fig. 26a), it is seen that the dominating contribution is shifted from the blade pressure side (right column, rear view of the fan) to the blade tip and ring region (left column, front view of the fan). This confirms that, in the presence of a radiator, the tonal content is reduced by the LN Vanes while the broadband content is increased or kept unchanged by the flow confinement due to the square casing of the radiator, which prevents the backflow from being radially redirected upstream. At the first BPF harmonic (Fig. 26b), the low noise geometry decreases the intensity of the spots aligned with the stator vanes, consistent with what was observed in Fig. 15b for the isolated fan. A slightly different pattern is seen in the near tip and ring area, where the contribution is shifted from the tip towards the whole blade span, with the effect of lowering the high intensity spots but globally increasing the noise levels. Finally, it is seen that the trace of the flow separation vortex structures at the blade pressure side is present at both frequencies and for both geometries, without a significative impact of the radiator installation in this configuration.

The directivity patterns at the BPF, its first two harmonics, and of the overall SPL in the frequency range $0 \leq f/BPF \leq 4$ are shown in Fig. 27. It is seen that the SPL at the BPF suffers from the same increase out of the fan rotational axis seen in Fig. 16 for the isolated fan configuration. Similarly, the SPL at the first two BPF harmonics follows the same trend, meaning that tonal noise is still dominated by the rotor-stator potential interaction noise at all the probes. Conversely, the OASPL is increased evenly

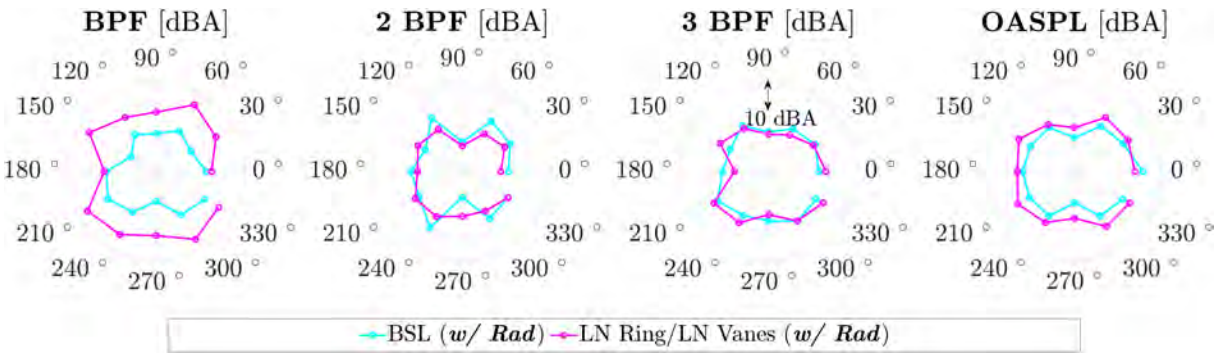

Figure 27: Directivity plots of the acoustic pressure at the BPF, the first two harmonics of the BPF, and the OASPL over the frequency range $0 \leq f/BPF \leq 4$ on the full cooling module configuration ($z/D = 0$).

at all the probes of interest, highlighting the inability of the LN Ring in mitigating the rotor-backflow interaction noise on the full cooling module configuration.

6 Conclusions

This study presents a numerical investigation of two aeroacoustic noise control strategies: (i) a change in the rotating ring geometry to mitigate the rotor-backflow interaction noise and (ii) an optimized stator vane azimuthal distribution to reduce rotor-stator potential interaction tonal noise. Both strategies are evaluated when applied to two configurations: an isolated axial flow cooling fan and the same fan installed within a full cooling module in which a radiator is added upstream. For both configurations, analyses are carried out at the respective best efficiency operating point. Three dimensional lattice-Boltzmann VLES flow simulations are used to quantify how the selected noise reduction technologies alter the aerodynamic and acoustic performances and what is the impact of the radiator installation on their effectiveness.

In the configuration without a radiator, shaping the rotating ring to redirect upstream recirculation effectively mitigates broadband noise by approximately 4 dBA. This broadband noise reduction is attributed to the mitigation of the rotor-backflow interaction because the flow is redirected radially. The LN Ring marginally impacts the rotor thrust but slightly shifts the operating point towards a volume flow rate that is 6% higher. Moreover, the torque is increased by about 10% as a result of the larger aerodynamic surface introduced by the LN Ring. When optimized stator vane azimuthal spacing is considered, tonal peaks at the blade passing frequency and harmonics are reduced respectively by 1.5 and 10 dBA due to the broader distribution of the acoustic energy among frequencies. This modification introduces marginal variations in the aerodynamic performance, only within 2%, thus not leading to any further operating point shift or efficiency decrease.

When the fan is installed within a casing with a radiator, the upstream flow confinement imposed by the radiator core and the casing limits the LN Ring ability to redirect the backflow radially, leading to a net increase of about 2 dBA in OASPL. Conversely, the optimized vane spacing continues to reduce tonal noise by up to 3 dBA, owing to its robust modulation of periodic loading fluctuations. Aerodynamic performance remains within $\pm$ 3% of the baseline, highlighting the lower sensitivity of the full cooling module configuration with respect to geometrical changes in the fan.

These findings highlight the importance of testing noise control geometries under installation: while tip ring shaping excels in the isolated fan configuration, its acoustic efficacy must be re-optimized in the presence of a flow confinement, whereas stator vane azimuthal spacing provides consistent tonal noise suppression regardless of upstream constraints. Future work should focus on designing noise reduction technologies for the rotor-backflow interaction noise that accounts for the radiator-induced flow field.

A Summary of previous validation and mesh sensitivity of simulations

This appendix summarizes the validation of the numerical simulations against the experiments and the mesh sensitivity study already presented in (Bellelli et al. 2025a; Bellelli et al. 2026). The reader is referred to these publications to gather further details on the experimental setup. Three different resolutions in terms of vox/D have been simulated for both the isolated fan and the full cooling module configuration. The isolated fan configuration has been tested with resolutions of 600, 1000, and 1200 vox/D, while the full cooling module configuration has been tested with resolutions of 300, 600, and 1200 vox/D. The isolated fan configuration has been simulated at free blowing (i.e. zero pressure rise) because the acoustic measurements are performed in an anechoic facility without a wind tunnel.

Fig. 28 presents the validation of the isolated fan configuration. Fig. 28a shows the ratio of mass flow rate through the fan section and torque obtained from the numerical simulations with the experimental ones. It also shows the SPL at the BPF and the first two harmonics, as well as the OASPL in terms of difference against the experimental values. It is seen that grid convergence for flow rate and torque is reached for the finest resolution case, as the extrapolated values are sufficiently close to the finest resolution. The mass flow rate differs by 1% with respect to the experimental one, while the torque is about 5% higher than the experimental one, similar to what was found by Lallier-Daniels et al. (2014). The tones at BPF and its first harmonic are predicted within 1.5 dBA at the finest resolution, with the BPF that is slightly overpredicted and the first harmonic that is slightly underpredicted. On the other hand, the second BPF harmonic is underpredicted by 6.5 dBA. Finally, the OASPL matches almost perfectly the experimental value at the finest resolution, while showing a 2 dBA underprediction at the medium

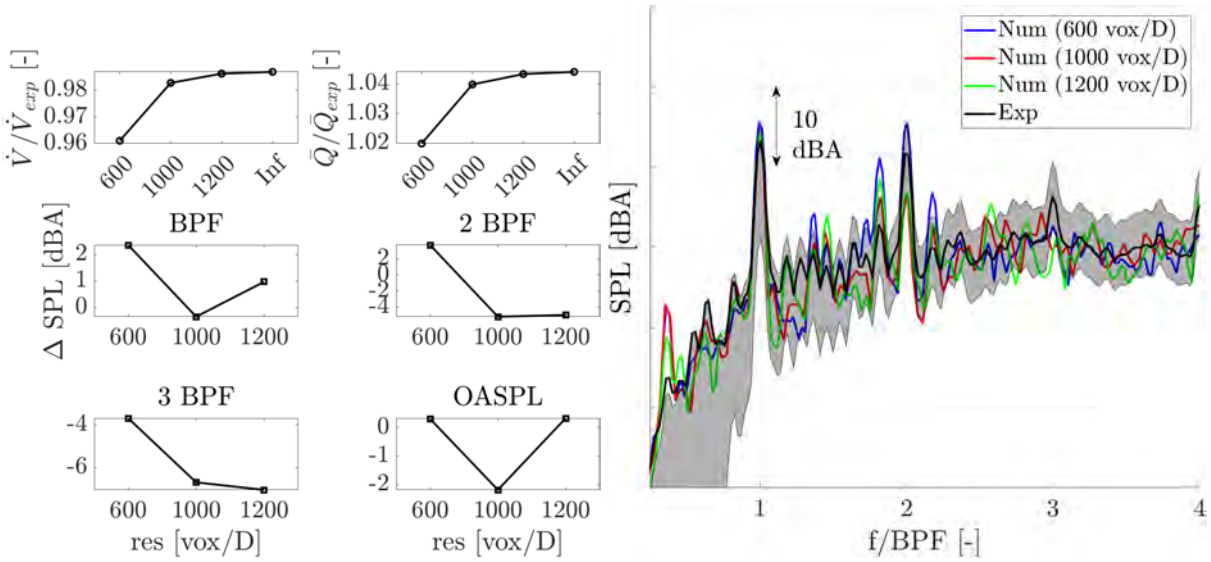

(a) (b)

Figure 28: Validation of the isolated fan configuration. (a): Mesh sensitivity study. (b): Sound Pressure Level in dBA obtained at $2.15D$ along the fan axis upstream.

resolution.

Fig. 28b compares the spectrum obtained at $x/D = -2.15$ along the fan axis upstream from the direct probe, at the three resolutions against the experimental one. The grey-shaded area represents the variability in the SPL during the complete sampling time of the experimental values (30 s) for windows of 10 revolutions, i.e. the same number of revolutions sampled in the numerical simulations; this has been done because of the notable differences between the sampling period of the simulations and experiments. It is seen that very few narrowband frequencies exceed the grey-shaded area, and that the tone at the second BPF harmonic is actually only a few dBA off the experimental signal, consistent with the findings of Amoiridis et al. (2022).

Fig. 29 presents the validation of the full cooling module configuration. Fig. 29a shows the mesh sensitivity study, highlighting that grid convergence is reached for the finest resolution case, as the extrapolated values are sufficiently close to the finest resolution (within 2%). The volume flow rate shows convergence, although resulting in a slight overestimation of the experimental value. On the other hand, the torque is characterized by a steeper variation between resolutions and is underestimated with respect to the corresponding experimental value. The differences in torque can be due to the difficulty in measuring a pure aerodynamic torque, while the discrepancies in flow rate might be associated with a slightly different recirculation pattern in the casing, since the simulated physical time is different from the experimental acquisition time. These issues have been previously assessed by Moreau and Sanjose (2016). The acoustic quantities are also grid independent, and the difference with respect to the experiments is

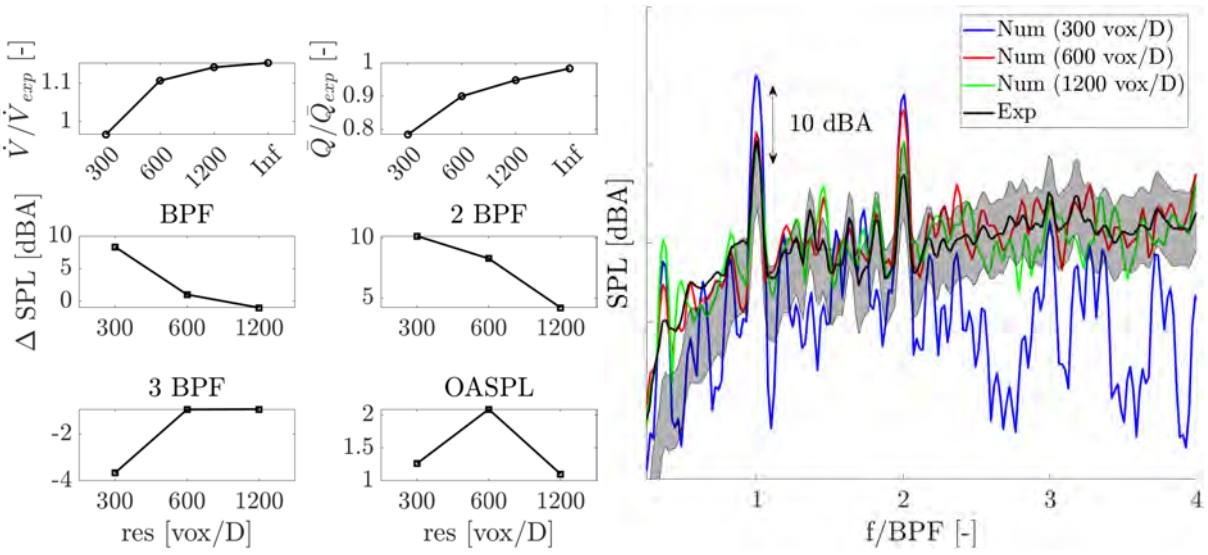

(a) (b)

Figure 29: Validation of the full cooling module configuration. (a): Mesh sensitivity study. (b): Sound Pressure Level in dBA obtained at $2.15D$ along the fan axis upstream.

within 3 dBA. In particular, the BPF and first harmonic are overestimated, while the second harmonic is underestimated; the OASPL instead shows less dependence to the resolution. This is in line with Fig. 28.

Fig. 29b compares the spectrum obtained at $x/D = -2.15$ along the fan axis upstream from the direct probe, at the three resolutions against the experimental one. The coarse resolution is seen not to be sufficient to properly capture any broadband content, while the tones up to the first BPF harmonic are overestimated; this might justify an OASPL which is not particularly different from the experiments. The medium and fine resolutions are instead able to correctly predict the broadband levels and are characterized by a less prominent tonal content at BPF and harmonics. Furthermore, the finest resolution shows better agreement at higher BPF harmonics.

Finally, Fig. 30 reports the complete experimental aerodynamic performance curves in terms of pressure and load coefficients of the isolated fan (blue) and of the radiator core (red), the latter obtained in the absence of the fan. The same plot also shows the φ and ψ values retained from the numerical simulations with the finest grid (1200 vox/D). The isolated fan is reported both at free blowing (Free) and at maximum efficiency (BEP) operating points while the full cooling module is reported only at free blowing since the pressure rise is created by the radiator core. As a matter of fact, the full cooling module simulation point lies exactly in the intersection between the isolated fan and radiator core experimental curves, confirming the accuracy of modeling the radiator core as a porous medium. All the numerical simulations are in line with the experiments, suggesting that the maximum efficiency operating point

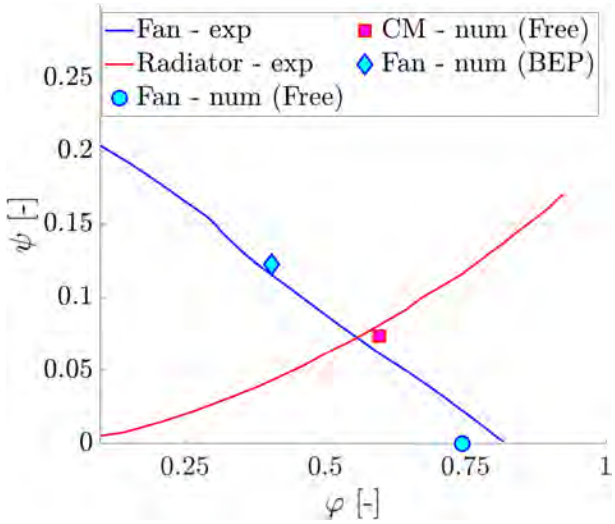

Figure 30: Aerodynamic performance curves of the isolated fan and of the radiator core.

yields accurate acoustic results as well, even though they were not experimentally tested in the acoustic facility.

References

Amoiridis, O. et al. (Jan. 2022). "Sound localization and quantification analysis of an automotive engine cooling module". In: *Journal of Sound and Vibration* 517, p. 116534. DOI: 10.1016/j.jsv.2021.116534.

Avallone, F., D. Ragni, and D. Casalino (June 2020). "On the effect of the tip-clearance ratio on the aeroacoustics of a diffuser-augmented wind turbine". In: *Renewable Energy* 152, pp. 1317–1327. DOI: 10.1016/j.renene.2020.01.064.

Bellelli, F., R. Arina, and F. Avallone (Jan. 2025a). "On the impact of operating condition and testing environment on the noise sources in an industrial engine cooling fan". In: *Applied Acoustics* 227, p. 110252. DOI: 10.1016/j.apacoust.2024.110252.

— (June 2025b). "Relevance of Radiator Installation on the Efficacy of Noise Reducation Strategies in an Industrial Engine Cooling Fan". In: *Forum Acusticum Euronoise 2025*. Forum Acusticum Euronoise 2025.

Bellelli, F. et al. (2026). "Aeroacoustic impact of heat exchanger installation in an industrial engine cooling module". In: *Applied Acoustics* 245, p. 111175.

Benedek, T., J. Vad, and B. Lendvai (Feb. 2022). "Combined acoustic and aerodynamic investigation of the effect of inlet geometry on tip leakage flow noise of free-inlet free-exhaust low-speed axial flow fans". In: *Applied Acoustics* 187, p. 108488. DOI: 10.1016/j.apacoust.2021.108488.

Bhatnagar, P. L., E. P. Gross, and M. Krook (May 1954). “A Model for Collision Processes in Gases. I. Small Amplitude Processes in Charged and Neutral One-Component Systems”. In: *Physical Review* 94.3, pp. 511–525. DOI: 10.1103/PhysRev.94.511.

Brooks, F., D. Pope, and A. Marcolini (1989). “Airfoil Self-Noise and Prediction”. In: *NASA Reference Publication 1218*.

Canepa, E., A. Cattanei, and F. Mazzocut Zecchin (July 2015). “Effect of the rotor–stator gap variation on the tonal noise generated by axial-flow fans”. In: *Applied Acoustics* 94, pp. 29–38. DOI: 10.1016/j.apacoust.2015.01.015.

Caro, S. and S. Moreau (June 2000). “Aeroacoustic modelling of low pressure axial flow fans”. In: *6th Aeroacoustics Conference and Exhibit*. Lahaina,HI,U.S.A.: American Institute of Aeronautics and Astronautics. DOI: 10.2514/6.2000-2094.

Casalino, D. et al. (June 2021). “Definition of a benchmark for low Reynolds number propeller aeroacoustics”. In: *Aerospace Science and Technology* 113, p. 106707. DOI: 10.1016/j.ast.2021.106707.

Cattanei, A. et al. (June 2021). “Effect of the uneven blade spacing on the noise annoyance of axial-flow fans and side channel blowers”. In: *Applied Acoustics* 177, p. 107924. DOI: 10.1016/j.apacoust.2021.107924.

Chapman, S. and T. G. Cowling (Jan. 1991). *The Mathematical Theory of Non-uniform Gases*. Publication Title: The Mathematical Theory of Non-uniform Gases ADS Bibcode: 1991mtnu.book.....C. Cambridge University Press.

Chen, H. et al. (Aug. 2003). “Extended Boltzmann Kinetic Equation for Turbulent Flows”. In: *Science* 301.5633, pp. 633–636. DOI: 10.1126/science.1085048.

Díaz, A. K. M. et al. (Sept. 2009). “Numerical prediction of tonal noise generation in an inlet vaned low-speed axial fan using a hybrid aeroacoustic approach”. In: *Proceedings of the Institution of Mechanical Engineers, Part C: Journal of Mechanical Engineering Science* 223.9, pp. 2081–2098. DOI: 10.1243/09544062JMES1426.

Duncan, P. and B. Dawson (Mar. 1974). “Reduction of interaction tones from axial flow fans by suitable design of rotor configuration”. In: *Journal of Sound and Vibration* 33.2, pp. 143–154. DOI: 10.1016/S0022-460X(74)80102-1.

— (Feb. 1975). “Reduction of interaction tones from axial flow fans by non-uniform distribution of the stator vanes”. In: *Journal of Sound and Vibration* 38.3, pp. 357–371. DOI: 10.1016/S0022-460X(75)80052-6.

Farassat, F. and G. P. Succi (1982). “The prediction of helicopter rotor discrete frequency noise”. In: *In: American Helicopter Society*, pp. 497–507.

Feng, J. et al. (2023). “A Numerical Investigation on the Influence of the Circular Ring on the Aerodynamic Noise Generated by a Cooling Fan”. In: *Fluid Dynamics & Materials Processing* 19.1, pp. 1–14. DOI: 10.32604/fdmp.2023.018275.

Ghodake, D. et al. (Nov. 2022). “Effect of Sweep on Axial Fan Noise Sources Using the Lattice Boltzmann Method”. In: *International Journal of Turbomachinery, Propulsion and Power* 7.4, p. 34. DOI: 10.3390/ijtpp7040034.

He, X. and L.-S. Luo (Dec. 1997). “Theory of the lattice Boltzmann method: From the Boltzmann equation to the lattice Boltzmann equation”. In: *Physical Review E* 56.6, pp. 6811–6817. DOI: 10.1103/PhysRevE.56.6811.

Jeong, J. and F. Hussain (Feb. 1995). “On the identification of a vortex”. In: *Journal of Fluid Mechanics* 285, pp. 69–94. DOI: 10.1017/S0022112095000462.

Kohout, D. and T. Hyhlík (Aug. 2020). “Influence of the shroud leading edge shape on the axial-fan noise”. In: *6th World Congress on Mechanical, Chemical, and Material Engineering*. 6th World Congress on Mechanical, Chemical, and Material Engineering. DOI: 10.11159/htff20.164.

Lallier-Daniels, D., S. Moreau, and M. Sanjose (Nov. 2014). “Aeroacoustics of a Low-Speed Free Tip Fan With a Complex Clearance Geometry”. In: *Volume 13: Vibration, Acoustics and Wave Propagation*. Montreal, Quebec, Canada: American Society of Mechanical Engineers, V013T16A004. DOI: 10.1115/IMECE2014-39160.

Lambora, A., K. Gupta, and K. Chopra (2019). “Genetic algorithm-A literature review”. In: *2019 international conference on machine learning, big data, cloud and parallel computing (COMITCon)*. IEEE, pp. 380–384.

Launder, B. E. and D. B. Spalding (1983). “The Numerical Computation of Turbulent Flows”. In: *Numerical prediction of flow, heat transfer, turbulence and combustion*, pp. 96–116.

Liang, Z. et al. (Jan. 2023). “Numerical and Experimental Investigations of Axial Flow Fan with Bionic Forked Trailing Edge”. In: *Machines* 11.2, p. 155. DOI: 10.3390/machines11020155.

Longhouse, R. (Oct. 1976). “Noise mechanism separation and design considerations for low tip-speed, axial-flow fans”. In: *Journal of Sound and Vibration* 48.4, pp. 461–474. DOI: 10.1016/0022-460X(76)90550-2.

Lowson, M. (1965). “The Sound Field for Singularities in Motion”. In: *Proceedings of the Royal Society of London. Series A, Mathematical and Physical Sciences*.

Lowson, M. (1970). “Theoretical Analysis of Compressor Noise”. In: *Proceedings of the Royal Society of London. Series A, Mathematical and Physical Sciences*.

Magne, S., S. Moreau, and A. Berry (Jan. 2015). “Subharmonic tonal noise from backflow vortices radiated by a low-speed ring fan in uniform inlet flow”. In: *The Journal of the Acoustical Society of America* 137.1, pp. 228–237. DOI: 10.1121/1.4904489.

Marsan, A. et al. (2018). “Tip Leakage Flow and its Implication on the Acoustic Signature of a Low-Speed Fan”. In: *FAN 2018*.

Mellin, R. C. and G. Sovran (Mar. 1970). “Controlling the Tonal Characteristics of the Aerodynamic Noise Generated by Fan Rotors”. In: *Journal of Basic Engineering* 92.1, pp. 143–154. DOI: 10.1115/1.3424923.

Moreau, S. and M. Roger (Jan. 2007). “Competing Broadband Noise Mechanisms in Low-Speed Axial Fans”. In: *AIAA Journal* 45.1, pp. 48–57. DOI: 10.2514/1.14583.

Moreau, S. and M. Sanjose (Jan. 2016). “Sub-harmonic broadband humps and tip noise in low-speed ring fans”. In: *The Journal of the Acoustical Society of America* 139.1, pp. 118–127. DOI: 10.1121/1.4939493.

Morfey, C. L. (May 1971). “Tone Radiation from an Isolated Subsonic Rotor”. In: *The Journal of the Acoustical Society of America* 49.5B, pp. 1690–1692. DOI: 10.1121/1.1912561.

Perot, F. et al. (June 2010). “Direct aeroacoustics predictions of a low speed axial fan”. In: *16th AIAA/CEAS Aeroacoustics Conference*. Stockholm, Sweden: American Institute of Aeronautics and Astronautics. DOI: 10.2514/6.2010-3887.

Pérot, F. et al. (2013). “Axial fan noise aeroacoustics predictions and inflow effect on tonal noise using LBM”. In: *CFD Canada 2013 Conference*.

Pestana, M. et al. (2018). “Investigation on the noise of an axial low Mach-number fan stage with a heterogeneous stator”. In: *FAN 2018*.

Piellard, M. et al. (June 2014). “Direct aeroacoustics simulation of automotive engine cooling fan system: effect of upstream geometry on broadband noise”. In: *20th AIAA/CEAS Aeroacoustics Conference*. Atlanta, GA: American Institute of Aeronautics and Astronautics. DOI: 10.2514/6.2014-2455.

Piwowarski, M. and D. Jakowski (Jan. 2023). “Areas of Fan Research—A Review of the Literature in Terms of Improving Operating Efficiency and Reducing Noise Emissions”. In: *Energies* 16.3, p. 1042. DOI: 10.3390/en16031042.

Qian, Y. H., D. D’Humières, and P. Lallemand (Feb. 1992). “Lattice BGK Models for Navier-Stokes Equation”. In: *Europhysics Letters (EPL)* 17.6, pp. 479–484. DOI: 10.1209/0295-5075/17/6/001.

Sanjose, M., D. Lallier-Daniels, and S. Moreau (June 2015). “Aeroacoustic Analysis of a Low-Subsonic Axial Fan”. In: *Volume 1: Aircraft Engine; Fans and Blowers; Marine*. Montreal, Quebec, Canada: American Society of Mechanical Engineers, V001T09A015. DOI: 10.1115/GT2015-43737.

Sharland, I. (July 1964). “Sources of noise in axial flow fans”. In: *Journal of Sound and Vibration* 1.3, pp. 302–322. DOI: 10.1016/0022-460X(64)90068-9.

Sortor, M. (Apr. 2011). “On-System Engine Cooling Fan Measurement as a Tool for Optimizing Cooling System Airflow Performance and Noise”. In: *SAE International Journal of Materials and Manufacturing* 4.1, pp. 1221–1230. DOI: 10.4271/2011-01-1169.

Sun, Z. et al. (Apr. 2023). “Cooling fan aerodynamic noise reduction with short inlet duct and its applicability”. In: *International Journal of Refrigeration* 148, pp. 117–130. DOI: 10.1016/j.ijrefrig.2023.01.013.

Teixeira, C. M. (Dec. 1998). “Incorporating Turbulence Models into the Lattice-Boltzmann Method”. In: *International Journal of Modern Physics C* 09.08, pp. 1159–1175. DOI: 10.1142/S0129183198001060.

Teruna, C. et al. (Jan. 2022). “A Numerical Study on Aircraft Noise Mitigation Using Porous Stator Concepts”. In: *Aerospace* 9.2, p. 70. DOI: 10.3390/aerospace9020070.

Tyler, J. M. and T. G. Sofrin (Jan. 1962). “Axial Flow Compressor Noise Studies”. In: *Pre-1964 SAE Technical Papers*. Vol. Pre-1964 SAE Technical Papers, p. 620532. DOI: 10.4271/620532.

Welch, P. (June 1967). “The use of fast Fourier transform for the estimation of power spectra: A method based on time averaging over short, modified periodograms”. In: *IEEE Transactions on Audio and Electroacoustics* 15.2, pp. 70–73. DOI: 10.1109/TAU.1967.1161901.

Whitaker, S. (1986). “Flow in porous media I: A theoretical derivation of Darcy’s law”. In: *Transport in Porous Media* 1.1, pp. 3–25. DOI: 10.1007/BF01036523.

Zhang, R. et al. (May 2011). “Lattice Boltzmann Approach for Local Reference Frames”. In: *Communications in Computational Physics* 9.5, pp. 1193–1205. DOI: 10.4208/cicp.021109.111110s.

Zhou, W. et al. (May 2023). “A Review of Bionic Structures in Control of Aerodynamic Noise of Centrifugal Fans”. In: *Energies* 16.11, p. 4331. DOI: 10.3390/en16114331.

Zhu, T. and T. H. Carolus (Mar. 2018). “Axial fan tip clearance noise: Experiments, Lattice–Boltzmann simulation, and mitigation measures”. In: *International Journal of Aeroacoustics* 17.1-2, pp. 159–183. DOI: 10.1177/1475472X17743627.

Zhu, T. et al. (Mar. 2018). “Rotating coherent flow structures as a source for narrowband tip clearance noise from axial fans”. In: *Journal of Sound and Vibration* 417, pp. 198–215. DOI: 10.1016/j.jsv.2017.11.014.